An Analytical Approach for Dealing With Explicit Physical Constraints in Excitation Optimization Problems of Dynamic Identification

Shifeng Huang, *Member, IEEE*, Fan Li, Xing Zhou, and Molong Duan, *Member, IEEE*

***Abstract*—Generating optimal excitation trajectories is crucial for ensuring that the observation matrix is well conditioned in robot dynamic identification. This task is a typical optimization problem involving explicit physical constraints defined by initial conditions (zero initial joint velocity and acceleration) and physical limits (joint position, velocity, and acceleration within specified bounds). Physical constraints complicate problem-solving, necessitating the use of heuristic or gradient-based iteration methods. Despite extensive study of this problem over many years, the success rate of finding feasible solutions that do not violate physical constraints within a limited number of iteration steps is lower than desired, and two major challenges remain: 1) a low success rate; and 2) high time consumption, which adversely affect practical applications. This article presents an analytical approach to address these physical constraints for excitation optimization. Feasible solutions are ensured through a deterministic calculation of the Fourier series-based parameterization rather than relying on iterative searches. Specifically, initial conditions are met by assigning offsets directly, while scaling and central-translation operations ensure adherence to physical limits. Our approach achieves a 100% success rate in generating physically executable excitation trajectories. Extensive experiments indicate that our approach has improved optimization efficiency by an order of magnitude compared to available methods, while delivering excellent excitation performance. For practitioners, our method renders excitation optimization a viable approach for time-critical payload identification tasks.**

***Index Terms*—Excitation trajectories, parameters identification, robot dynamics.**

Received 31 October 2024; accepted 6 February 2025. Date of publication 18 February 2025; date of current version 20 March 2025. This work was supported in part by National Key R&D Program of China under Grant 2023YFB4703800, in part by HKUSTHKUST(GZ) Cross-campus Collaborative Research Scheme under the "1+1+1" Joint Funding Program, as well as HKUST Frontier Technology Research for Joint Institutes with Industry Scheme under Grant OKT24EG07. This article was recommended for publication by Associate Editor S. Weiss and Editor T. Bretl upon evaluation of the reviewers' comments. *(Corresponding author: Molong Duan.)*

Shifeng Huang is with the Hong Kong University of Science and Technology, Hong Kong SAR 999077, China, and also with the Foshan Huashu Robot Company Ltd, Foshan 528200, China (e-mail: fenghkust@gmail.com).

Fan Li is with the Department of Computer Science, University of Exeter, Exeter EX4 4QF, U.K, and also with the Central South University, Changsha 410000, China (e-mail: f.li@exeter.ac.uk).

Xing Zhou is with the Foshan Institute of Intelligent Equipment Technology, Foshan 528234, China (e-mail: zhouxing@hzncc.com).

Molong Duan is with the Hong Kong University of Science and Technology, 999077, Hong Kong, and also with the HKUST Shenzhen-Hong Kong Collaborative Innovation Research Institute, Shenzhen 518000, China (e-mail: duan@ust.hk).

This article has supplementary downloadable material available at https://doi.org/10.1109/TRO.2025.3543296, provided by the authors.

Digital Object Identifier 10.1109/TRO.2025.3543296

Nomenclature

Notations	Definition
$\dot{x}$	first derivative of x with respect to time.
$\ddot{x}$	second derivative of x with respect to time.
$\lvert \cdot \rvert$	absolute value of a scalar.
$\mathrm{cond}(\cdot)$	condition number of a matrix.
$\det(\cdot)$	determinant of a matrix.
$\max(\cdot)$	maximum value of a set or sequence.
$\min(\cdot)$	minimum value of a set or sequence.
$x := m$	x is defined to be equal to m.
$x \leftarrow m$	assign the value of m to x.

I. Introduction

Advanced robot features, such as compliant manipulation [1], physical human-robot interaction [2], time-optimal trajectory planning [3], high-precision servo control [4], walking balance [5], and more, are made possible by dynamic models. Within the scope of model identification, generating appropriate motion trajectories (referred to as excitation trajectories) is essential for exciting dynamic behavior of model parameters through demonstrating significant force/torque acting on the robot joints, while minimizing the perturbation of measurement noise and unmodeled dynamics for parameter estimation. This issue involves a very specific concept known as excitation optimization [6].

For a real-world robot, the joint position, velocity, and acceleration should stay within allowable bounds when generating excitation trajectories, which define the constraints of physical limits. In addition, the initial velocity and acceleration should be zero due to the servo driver's finite control bandwidth and the effects of structural resonance, forming the initial conditions. In this article, these initial conditions and physical limits collectively define the physical constraints that govern the excitation optimization task. For this reason, excitation optimization is a constrained optimization problem that requires ensuring the observation matrix in linear regression is well conditioned while also adhering to physical constraints. In this context, its solution requires resorting to iterative search algorithms, such as heuristics and gradient-based optimization. The investigation into finding optimal excitation trajectories for the dynamic identification of robots has now been ongoing for over 30 years [7]. Nevertheless, multivariate optimization with constraints remains a challenging task, and this issue has long plagued robot excitation optimization, resulting in the following limitations.

1) A feasible solution may not be found within a limited number of iteration steps, leading to optimization failure.
2) Finding a feasible solution might take considerable computational efforts for excitation optimization.

An infeasible solution could lead to abnormal accidents, such as collisions, motor overloads, or mechanical vibrations. The manufacturing industry typically places high demands on reliability, aiming for a success rate close to 100%, as failures can result in production downtime and increased costs. Therefore, the generation of optimal excitation trajectories is usually performed with offline routines and is only acceptable for model identification of the robot body model, which naturally raises the question of how to address payload identification tasks in a time-critical on-site operational environment. Practice shows that commercially available robots, such as KUKA iiwa, ABB, Yaskawa [8], [9], [10], etc., usually run pose-independent excitation trajectories when performing the payload identification function, i.e., these trajectories are feasible but not optimized.

This article aims to propose a practical excitation optimization method that is both computationally efficient and capable of reliably finding feasible excitation trajectories (i.e., without violating physical constraints).

A. Related Work

Armstrong [11] is widely recognized as a pioneer in determining the optimal excitation trajectories for robots. He achieved this by finding the optimal sequence of joint accelerations and deriving the velocities and positions through numerical integration. However, this method lacks an explicit parameterization for excitation trajectories, and its implementation is cumbersome. Three years after Armstrong's findings, Gautier and Khalil [7] introduced a piecewise fifth-order polynomial as an explicit parameterization of the excitation trajectory. They also highlighted the impact of a well-equilibrated observation matrix on determining the upper bound of parameter estimation uncertainty. However, altering intermediate waypoints would modify the entire polynomial trajectory. Rackl et al. [12] proposed the use of B-splines with local adjustability as a solution for excitation trajectory parameterization. Moreover, B-splines were employed as a type of excitation trajectory for parameter estimation in a humanoid robot, as demonstrated by Bonnet et al. [13]. In order to implement customized model identification on commercial robots with nonopen controllers, Pedrocchi et al. [14] developed excitation trajectories that depend only on teaching points and programmed velocities; nevertheless, it is worth noting that these trajectories might compromise the accuracy of parameter estimation. To address this issue, a task-related excitation trajectory in a subspace was introduced. Pejman et al. [15] suggested using the Schroeder-phased harmonic sequence to parameterize the excitation trajectories. In addition, the correlation among all robot joints was considered to increase the effective coverage rate of the trajectory space (a hyperspace composed of position, velocity, and acceleration).

The method of parameterizing excitation trajectories using finite Fourier series was first introduced by Swevers in 1996 [16] and has been the most commonly used type ever since [17]. It has several benefits (refer to Fig. 1) as follows.

1) Periodic motion allows for an improvement in the signal-to-interference-plus-noise ratio (SINR) via time-domain data averaging.
2) A statistical analysis of the measurement noise can be performed for multicycle operation, which is crucial for accurate identification, such as maximum likelihood estimation [18], weighted least squares [19], etc.
3) The excitation bandwidth can be specified to avoid the lowest resonance frequency of the structural flexibility of robots.
4) Data processing is more rigorous, allowing for the calculation of joint velocities and accelerations by windowing the spectrum in the frequency-domain.

While the Fourier series-based parameterization offers many strengths, it is evident that using optimization techniques to determine appropriate Fourier coefficients in order to satisfy initial conditions poses significant challenges, as demonstrated by the experiments conducted by Nicholas et al. [20]. Therefore, a hybrid trajectory was proposed [21] in which the constant term of the Fourier series is replaced by a fifth-order polynomial, denoted as Fourier-polynomial hybrid parameterization in our article. This approach leverages fifth-order polynomials in trajectory planning to meet initial conditions effectively and is widely used [22]. Nevertheless, it introduces nonspecified frequency components, which negates many of the benefits of the Fourier series.

The approach to generating optimal excitation trajectories, regardless of the parameterization method, is commonly formulated as an optimization problem with explicit constraints. Practitioners often utilize well-established optimization tools, such as the MATLAB built-in function fmincon [23], to find optimal excitation trajectories. Popular optimization solvers include the interior-point (IP) [24] and sequential quadratic programming (SQP) [17] algorithms. Some scholars have also tried to solve the excitation optimization problem using genetic algorithms (GAs) [25], particle swarm optimization (PSO) [26], particle grey wolf optimization [27], and others. Those population-based heuristic algorithms typically require supplementary strategies, such as penalty functions and separation methods [28], to handle constraint problems. However, heuristic algorithms are inherently stochastic, whereas gradient-based methods are sensitive to initial guesses, which renders the search for feasible solutions probabilistic and introduces some level of uncertainty.

In recent years, the time-consuming drawback of generating optimal excitation trajectories has gained attention. Nicholas [20] used the Hadamard's inequality to simplify the complexity of calculating the optimization criterion; however, this new criterion lacks direct correlation with the uncertainty of parameter estimation. In practice, optimization criteria like the logarithm of the determinant (known as the d-optimality criterion [29]) or the condition number [30] of the observation matrix are more commonly used. These criteria provide an upper bound on the uncertainty of parameter estimation. In light of this, a phased optimization procedure was proposed [17] to achieve a balance between the robustness of parameter identification and

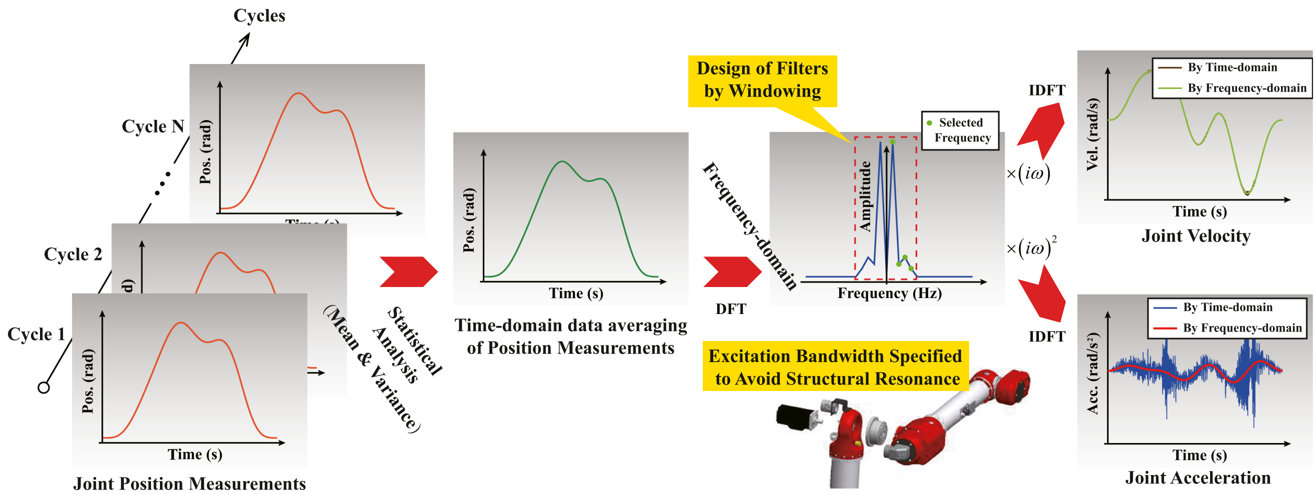

Fig. 1. Illustration of data processing of the excitation trajectories based on finite Fourier series, also known as Fourier series-based parameterization. The frequency-domain filter by a rectangular window selects the specified frequency components, and the spectrum is set to zero at all other frequencies. $(i\omega)$ is a differentiator in the frequency-domain, and i is the imaginary number. DFT represents the discrete Fourier transform, while its inverse operation is IDFT.

the efficiency of excitation trajectory generation. Specifically, the Hadamard's inequality-based criterion was first employed to generate the initial guess, and then an iterative search for the optimal solution was performed based on minimizing the condition number. There has also been a trend in the robotics community toward using machine learning methods to bypass the high time consumption faced in solving constrained optimization problems. Marija et al. [31] leveraged a generative adversarial network to mitigate the computationally intensive challenge of generating long excitation trajectories. Duan et al. [32] adopted a supervised learning approach to facilitate the rapid generation of excitation trajectories for payload identification tasks. However, these machine learning methods for generating excitation trajectories face real-world challenges and share some common problems as follows.

1) They require a large number of datasets for training, and data collection can be time-consuming.
2) Creating a high-quality training dataset is challenging due to the dependence of the observation matrix on joint positions, velocities, and accelerations.
3) They have not eliminated the need for classical excitation trajectory optimization methods, as generating the training datasets still depends on a heuristic or gradient-based optimization solver.
4) The trained model risks generating excitation trajectories with high condition numbers and violating physical constraints, while its generalization performance remains limited.

B. Our Work and Contributions

In this article, we propose an analytical approach to calculate feasible solutions in excitation optimization problems. We reformulated the expression of the finite Fourier series while preserving its foundational structure. The way we do it divides the finite Fourier series into main and offset trajectories, and adds offset terms for velocity and acceleration. We can assign these offsets directly to meet the requirements of the initial conditions; this elegant solution is made possible by leveraging the 90-degree phase difference characteristic between the sine and cosine functions. We also perform a scaling operation on the Fourier coefficients to adhere to the physical limits on both joint velocity and acceleration. Furthermore, a central-translation operation is implemented to satisfy the bounds on position. For completeness, we incorporated the analytical constraint-handling method within a teaching–learning-based optimization (TLBO) [33] framework to demonstrate its implementation in excitation optimization. TLBO is a population-based heuristic optimization algorithm that does not have any algorithm-specific parameters,[1] making it easy to implement. Notably, our analytical constraint-handling approach is not limited to any particular optimization algorithm.

The major contributions are as follows.

1) An analytical approach for handling physical constraints in excitation optimization is proposed, ensuring the deterministic calculation of feasible solutions. The discovery of feasible solutions in existing methods relies on iterative search, which introduces inherent uncertainty.
2) Our method achieves a 100% success rate in generating excitation trajectories that do not violate physical constraints. Moreover, each joint always has a component of motion that reaches its specified bounds, enhancing the coverage rate of the trajectory space. Existing methods take a long time to find feasible solutions, while our approach guarantees that all candidate solutions are feasible, leading to significantly faster optimization.
3) Our method facilitates the application of excitation optimization in time-critical payload identification tasks. It can also effectively reduce the time burden on robot manufacturers when identifying robot body models offline in large-scale production.

[1] Algorithm-specific parameters [34] (for example, PSO needs inertia weight, social and cognitive parameters, while GA requires crossover and mutation rates) pose operational challenges, as their tuning may impact the optimization solver's effectiveness.

The rest of this article is organized as follows. Section II gives some basic preliminaries and formulates the excitation optimization problems. Section III details the proposed analytical approach for finding feasible solutions, ensuring that the generated excitation trajectories adhere to physical constraints. Section IV presents a TLBO framework that incorporates our constraint-handling method to implement excitation optimization. Section V demonstrates the experimental verifications. Finally, Section VI concludes this article.

II. Preliminaries and Problem Formulation

The finite Fourier series serves as the basis for parameterizing the excitation trajectories in this study and is given by the following equation:

$$q_k(t) = \sum_{i=1}^{L}\left(\frac{a_i^k}{i\omega_f}\sin(i\omega_f t) - \frac{b_i^k}{i\omega_f}\cos(i\omega_f t)\right) + q_{k,0}, \quad (1)$$

where t represents time, q_k $(k = 1, \ldots, n)$ is the position of joint k in an n degree-of-freedom (DOF) robot, $q_{k,0}$ is a constant offset of the position trajectory, and ω_f is the fundamental frequency that is preset and uniform across all excited joints. This L-term Fourier series specifies a periodic function with a period of $T_f = 2\pi/\omega_f$. a_i^k and b_i^k are the ith-order sine and cosine coefficients for joint k, respectively.

The excitation optimization can be defined as

$$\begin{aligned}
&\underset{\aleph}{\text{minimize}} \quad J_1 = \text{cond}(\boldsymbol{H}_b)\\
&\text{s.t.}\\
&\text{physical limits}\begin{cases} q_{k,\min} \le q_k(t) \le q_{k,\max} & \forall\, k, t\\ |\dot{q}_k(t)| \le \dot{q}_{k,\max} & \forall\, k, t\\ |\ddot{q}_k(t)| \le \ddot{q}_{k,\max} & \forall\, k, t\end{cases}\\
&\text{initial conditions}\begin{cases} \dot{q}_k(0) = 0 & \forall\, k\\ \ddot{q}_k(0) = 0 & \forall\, k\end{cases}
\end{aligned} \quad (2)$$

with $\aleph \in \mathbb{R}^{(2L+1)n_\rho}$ as the set of the decision variables for n_ρ joints. Each Fourier series comprises $2L+1$ coefficients to be optimized, including a_i^k, b_i^k, and $q_{k,0}$ $(i = 1, \ldots, L)$. $q_{k,\min}$ and $q_{k,\max}$ denote the allowed minimum and maximum motion ranges for joint k, respectively. $\dot{q}_{k,\max}$ and $\ddot{q}_{k,\max}$ denote the bounds on velocity and acceleration for joint k, respectively. In practice, the excitation optimization is implemented at N_m preset discrete time instants rather than over a continuous time interval $[0, T_f]$. $\boldsymbol{H}_b \in \mathbb{R}^{n_\rho N_m \times n_b}$ refers to the observation (or regressor) matrix used in the linear regression for dynamic parameter identification, which is stacked from the N_m motion data points as

$$\boldsymbol{H}_b = \begin{bmatrix} \boldsymbol{W}_b(\boldsymbol{q}(t_1), \dot{\boldsymbol{q}}(t_1), \ddot{\boldsymbol{q}}(t_1))\\ \boldsymbol{W}_b(\boldsymbol{q}(t_2), \dot{\boldsymbol{q}}(t_2), \ddot{\boldsymbol{q}}(t_2))\\ \vdots\\ \boldsymbol{W}_b(\boldsymbol{q}(t_{N_m}), \dot{\boldsymbol{q}}(t_{N_m}), \ddot{\boldsymbol{q}}(t_{N_m}))\end{bmatrix} \in \mathbb{R}^{n_\rho N_m \times n_b} \quad (3)$$

where $\boldsymbol{W}_b \in \mathbb{R}^{n_\rho \times n_b}$ is a task-related dynamic model. Specifically, $\boldsymbol{W}_b$ can be either a robot body model [35] or a payload model [36], and its form also depends on the friction model employed [37], [38]. Therefore, the dimension n_b of the base parameter set [39] is also task-related. The detailed knowledge of dynamic models and their associated parameters is beyond the scope of this article, but can be found in [40]. t_j denotes the jth time instant and $\boldsymbol{q} \in \mathbb{R}^n$ is the joint position.

An excitation trajectory using the Fourier-polynomial hybrid parameterization, which can eliminate the constraints of the initial conditions defined in (2), is expressed as follows:

$$q_k(t) = \sum_{i=1}^{L}\left(\frac{a_i^k}{i\omega_f}\sin(i\omega_f t) - \frac{b_i^k}{i\omega_f}\cos(i\omega_f t)\right) + q_{k,p}(t) \quad (4)$$

with

$$q_{k,p}(t) = \sum_{j=0}^{5} c_j^k (t - (z-1)T_f)^j \quad (5)$$

where c_j^k is the $(j+1)$th fifth-order polynomial coefficient of joint k, and the zth motion cycle is calculated as

$$z = \left\lceil \frac{t}{T_f} \right\rceil \quad (6)$$

where $\lceil\cdot\rceil$ denotes the ceiling function (e.g., $\lceil 0.2 \rceil = 1$).

Furthermore, c_j^k $(j = 0, \ldots, 5)$ can be fully expressed in terms of the coefficients a_i^k and b_i^k $(i = 1, \ldots, L)$ as

$$\begin{cases}
c_0^k = 0\\
c_1^k = -\sum_{i=1}^{L} a_i^k\\
c_2^k = -\frac{\omega_f}{2}\sum_{i=1}^{L} i b_i^k\\
c_3^k = \frac{1}{T_f^2}\left(10\sum_{i=1}^{L} a_i^k + \omega_f T_f \sum_{i=1}^{L} i b_i^k\right)\\
c_4^k = -\frac{1}{2T_f^3}\left(30\sum_{i=1}^{L} a_i^k + \omega_f T_f \sum_{i=1}^{L} i b_i^k\right)\\
c_5^k = \frac{6}{T_f^4}\sum_{i=1}^{L} a_i^k.
\end{cases} \quad (7)$$

Therefore, the original optimization problem (2) is simplified to

$$\begin{aligned}
&\underset{\aleph^\dagger}{\text{minimize}} \quad J_1 = \text{cond}(\boldsymbol{H}_b)\\
&\text{s.t.}\\
&\text{physical limits}\begin{cases} q_{k,\min} \le q_k(t) \le q_{k,\max}, & \forall\, k, t\\ |\dot{q}_k(t)| \le \dot{q}_{k,\max}, & \forall\, k, t\\ |\ddot{q}_k(t)| \le \ddot{q}_{k,\max}, & \forall\, k, t\end{cases}
\end{aligned} \quad (8)$$

and the dimensions of the decision variables $\aleph^\dagger \in \mathbb{R}^{(2~L)n_\rho}$ are thus reduced, requiring only $2L$ coefficients to be optimized per joint, i.e., a_i^k and b_i^k $(i = 1, \ldots, L)$.

The Hadamard's inequality adopted by Nicholas [20] simplifies the complexity of calculating the optimization criterion by estimating the upper bound of the determinant of $\boldsymbol{H}_b^{\mathrm{T}}\boldsymbol{H}_b$ as

$$\det(\boldsymbol{H}_b^{\mathrm{T}}\boldsymbol{H}_b) \leq \prod_{c=1}^{n_b}\sum_{k=1}^{n_\rho N_m} \boldsymbol{H}_b[k,c]^2, \tag{9}$$

where $\boldsymbol{H}_b[k,c]$ denotes the kth element of the cth column of the observation matrix $\boldsymbol{H}_b$. Accordingly, a new objective function J_2 is defined as

$$J_2 = \frac{1}{\prod_{c=1}^{n_b}\sum_{k=1}^{n_\rho N_m} \boldsymbol{H}_b[k,c]^2}. \tag{10}$$

Following the discussion of objective functions[2] and constraints, the optimization problem for excitation trajectories is typically formulated in three ways as follows.

1) Fourier series-based parameterization with the objective function J_1, subject to both initial conditions and physical limits, as is done in [43].
2) Fourier-polynomial hybrid parameterization with the objective function J_1, subject to physical limits only, as is done in [21].
3) Fourier series-based parameterization with the objective function J_2, subject to both initial conditions and physical limits, as is done in [20].

For clarity, we refer to these three types of optimization problems as Problem 1, Problem 2, and Problem 3, respectively.

III. Analytical Approach for Dealing With Physical Constraints

In this section, we present an analytical approach for handling physical constraints in excitation optimization. Specifically, the finite Fourier series in (1) is reformulated as

$$q_k(t) = \phi_1(t) + \phi_2(t) \tag{11}$$

with

$$\phi_1(t) = \sum_{i=1}^{L}\left(\frac{a_i^k}{i\omega_f}\sin(i\omega_f t) - \frac{b_i^k}{i\omega_f}\cos(i\omega_f t)\right) \tag{12}$$

and

$$\phi_2(t) = q_{k,0} - \frac{\dot{q}_{k,0}}{\omega_f}\sin(\omega_f t) + \frac{\ddot{q}_{k,0}}{\omega_f^2}\cos(\omega_f t), \tag{13}$$

where $\phi_1(t)$ is referred to as the main trajectory, $\phi_2(t)$ is named the offset trajectory, and $\dot{q}_{k,0}$ and $\ddot{q}_{k,0}$ represent specially designed offsets on the velocity and acceleration trajectories, respectively. The reformulated finite Fourier series is split into these two parts, with the underlying philosophy being to use the offset trajectory to handle the initial conditions. In addition, $q_{k,0}$, $\dot{q}_{k,0}$, and $\ddot{q}_{k,0}$ are classified as passive decision variables, while a_i^k and b_i^k $(i = 1,\ldots,L)$ are designated active decision variables. This naming convention is grounded in the fact that the values of the passive decision variables depend on the active ones, and the implementation procedure is described as follows.

Consider the initial conditions for joint acceleration

$$\ddot{q}_k(0) = \sum_{i=1}^{L} i\omega_f b_i^k - \ddot{q}_{k,0} = 0. \tag{14}$$

Let the offset on the acceleration trajectory be

$$\ddot{q}_{k,0} \leftarrow \sum_{i=1}^{L} i\omega_f b_i^k \tag{15}$$

then (11) satisfies the initial conditions for acceleration.

Similarly, consider the initial conditions for joint velocity

$$\dot{q}_k(0) = \sum_{i=1}^{L} a_i^k - \dot{q}_{k,0} = 0. \tag{16}$$

Let the offset on the velocity trajectory be

$$\dot{q}_{k,0} \leftarrow \sum_{i=1}^{L} a_i^k \tag{17}$$

then (11) satisfies the initial conditions for velocity.

Therefore, by assigning suitable values to the offsets on the velocity and acceleration trajectories, the initial conditions in the excitation optimization problem can be efficiently solved without the necessity of introducing a fifth-order polynomial. Consequently, our trajectory retains all the benefits of the finite Fourier series.

Remark 1: The uncoupled calculations of the velocity offset $\dot{q}_{k,0}$ and the acceleration offset $\ddot{q}_{k,0}$ benefit from the 90° phase difference between the sine and cosine functions.

Furthermore, after modifying $\ddot{q}_{k,0}$ and $\dot{q}_{k,0}$ in accordance with (15) and (17), respectively, we define the characteristic quantities of the excitation trajectory as follows:

$$\begin{cases} Q_{k,\max} = \max(q_k(t)) \\ Q_{k,\min} = \min(q_k(t)) \\ \dot{Q}_{k,|\max|} = \max(|\dot{q}_k(t)|) \\ \ddot{Q}_{k,|\max|} = \max(|\ddot{q}_k(t)|). \end{cases} \tag{18}$$

Note that multiplying all coefficients in (11) by the same scaling factor will alter the extremum of the excitation trajectory without affecting the already satisfied initial conditions. In addition, the offset $q_{k,0}$ can translate the entire excitation trajectory without altering its geometric shape (i.e., the first and second derivatives remain unchanged). Therefore, the physical limits can be analytically satisfied through scaling and translation operations.

A. Scaling

Given that the feasible intervals for velocity and acceleration are symmetric about zero, define a velocity scaling factor $\lambda_{k,V}$ and an acceleration scaling factor $\lambda_{k,A}$ as

$$\lambda_{k,V} = \frac{\dot{q}_{k,\max}}{\dot{Q}_{k,|\max|}} \tag{19}$$

[2]Various approaches for evaluating the objective function, such as the d-optimality criterion or variants of cond($\boldsymbol{H}_b$) that incorporate singular values [41] or weighted multiple observation matrices [42], are irrelevant to the constraint-handling method and are thus not discussed further.

and

$$\lambda_{k,A} = \frac{\ddot{q}_{k,\max}}{\ddot{Q}_{k,|\max|}}. \tag{20}$$

Furthermore, define a position scaling factor $\lambda_{k,P}$ as

$$\lambda_{k,P} = \frac{q_{k,\max} - q_{k,\min}}{Q_{k,\max} - Q_{k,\min}} \tag{21}$$

and then define a comprehensive scaling factor λ_k as

$$\lambda_k = \min(\{\lambda_{k,P}, \lambda_{k,V}, \lambda_{k,A}\}). \tag{22}$$

Implement a scaling operation on the currently provided Fourier coefficients, i.e.,

$$\breve{a}_i^k := \lambda_k a_i^k, \quad \breve{b}_i^k := \lambda_k b_i^k$$
$$\breve{q}_{k,0} := \lambda_k q_{k,0}, \quad \dot{\breve{q}}_{k,0} := \lambda_k \dot{q}_{k,0}, \quad \ddot{\breve{q}}_{k,0} := \lambda_k \ddot{q}_{k,0}. \tag{23}$$

Use $\breve{a}_i^k$, $\breve{b}_i^k$ $(i = 1, \dots, L)$, $\breve{q}_{k,0}$, $\dot{\breve{q}}_{k,0}$, and $\ddot{\breve{q}}_{k,0}$ as coefficients of the scaled finite Fourier series and name the scaled excitation trajectory $\breve{q}_k(t)$. The relationship

$$\breve{q}_k(t) = \lambda_k q_k(t) \tag{24}$$

holds, leading to the following equations:

$$\begin{cases} \breve{Q}_{k,\max} = \max(\breve{q}_k(t)) = \lambda_k Q_{k,\max} \\ \breve{Q}_{k,\min} = \min(\breve{q}_k(t)) = \lambda_k Q_{k,\min} \\ \dot{\breve{Q}}_{k,|\max|} = \max(|\dot{\breve{q}}_k(t)|) = \lambda_k \dot{Q}_{k,|\max|} \\ \ddot{\breve{Q}}_{k,|\max|} = \max(|\ddot{\breve{q}}_k(t)|) = \lambda_k \ddot{Q}_{k,|\max|}. \end{cases} \tag{25}$$

The equation

$$\max\left(\frac{\breve{Q}_{k,\max} - \breve{Q}_{k,\min}}{q_{k,\max} - q_{k,\min}}, \frac{\dot{\breve{Q}}_{k,|\max|}}{\dot{q}_{k,\max}}, \frac{\ddot{\breve{Q}}_{k,|\max|}}{\ddot{q}_{k,\max}}\right) = 1 \tag{26}$$

holds. Therefore, the scaled excitation trajectory ensures that the magnitude of changes in position, velocity, and acceleration of joint k do not exceed their specified bounds, and at least one of them will reach its limits.

Remark 2: Maximizing the range of joint motion can improve the generalization performance of dynamic identification results. In addition, higher joint velocities and accelerations are more effective at exciting the dynamic behavior of model parameters and increasing the SINR of measurements [29]. Consequently, the design philosophy of excitation trajectories is to maximize the variations in position, velocity, and acceleration within their allowable intervals.

B. Central Translation

Although the scaling operation limits the change in joint position to a specified range, it does not guarantee that the actual position values stay within the allowable intervals. To address this, we propose to implement a central-translation operation on the joint position $\breve{q}_k(t)$ as follows.

The center point of the feasible interval for the joint position is denoted as

$$q_{k,ce} = \frac{q_{k,\max} + q_{k,\min}}{2}. \tag{27}$$

Algorithm 1: An Analytical Constraint-Handling Method for Excitation Optimization.

- **Input**: Original coefficients a_i^k, b_i^k, $q_{k,0}$, $\dot{q}_{k,0}$, and $\ddot{q}_{k,0}$ $(i = 1, \dots, L)$ of the finite Fourier series
- **Output**: Modified coefficients a_i^k, b_i^k, $q_{k,0}$, $\dot{q}_{k,0}$, and $\ddot{q}_{k,0}$ $(i = 1, \dots, L)$ of the finite Fourier series

// Regarding initial conditions
Correct the offsets $\dot{q}_{k,0}$ and $\ddot{q}_{k,0}$ as

$$\dot{q}_{k,0} \leftarrow \sum_{i=1}^{L} a_i^k \qquad \ddot{q}_{k,0} \leftarrow \sum_{i=1}^{L} i\omega_f b_i^k.$$

// Regarding physical limits
// Scaling operation:
Calculate the scaling factor λ_k // (19) to (22)
Scaling Fourier coefficients

$$a_i^k \leftarrow \lambda_k a_i^k, \quad b_i^k \leftarrow \lambda_k b_i^k \quad \forall i = 1, \dots, L$$
$$q_{k,0} \leftarrow \lambda_k q_{k,0}, \quad \dot{q}_{k,0} \leftarrow \lambda_k \dot{q}_{k,0}, \quad \ddot{q}_{k,0} \leftarrow \lambda_k \ddot{q}_{k,0}.$$

// Central-translation operation:
Calculate the deviation $\delta_{k,ce}$ // (27) to (29)
Translate the position offset as

$$q_{k,0} \leftarrow q_{k,0} - \delta_{k,ce}.$$

Return a_i^k, b_i^k, $q_{k,0}$, $\dot{q}_{k,0}$, and $\ddot{q}_{k,0}$ $(i = 1, \dots, L)$

The center point of the position trajectory $\breve{q}_k(t)$ is denoted as

$$\breve{Q}_{k,ce} = \frac{\breve{Q}_{k,\max} + \breve{Q}_{k,\min}}{2} \tag{28}$$

and the deviation between $\breve{Q}_{k,ce}$ and $q_{k,ce}$ is calculated as

$$\delta_{k,ce} = \breve{Q}_{k,ce} - q_{k,ce}. \tag{29}$$

Furthermore, translate the offset $\breve{q}_{k,0}$ on the position trajectory as

$$\breve{q}_{k,0}^* := \breve{q}_{k,0} - \delta_{k,ce}. \tag{30}$$

In this context, the finite Fourier series with coefficients $\breve{a}_i^k$, $\breve{b}_i^k$, $\breve{q}_{k,0}^*$, $\dot{\breve{q}}_{k,0}$, and $\ddot{\breve{q}}_{k,0}$ $(i = 1, \dots, L)$ has fully satisfied the physical constraints. For consistency in notation, the coefficients of the finite Fourier series are reassigned as

$$a_i^k \leftarrow \breve{a}_i^k, \quad b_i^k \leftarrow \breve{b}_i^k$$
$$q_{k,0} \leftarrow \breve{q}_{k,0}^*, \quad \dot{q}_{k,0} \leftarrow \dot{\breve{q}}_{k,0}, \quad \ddot{q}_{k,0} \leftarrow \ddot{\breve{q}}_{k,0}. \tag{31}$$

The proposed analytical approach for handling explicit physical constraints in the optimization of excitation trajectories is summarized in Algorithm 1.

IV. TLBO-Based Excitation Optimization With the Analytical Constraint-Handling Method

In this section, we introduce how to use the analytical constraint-handling method along with the TLBO algorithm to generate optimal excitation trajectories. The use of TLBO in our optimization framework is based on the following considerations.

1) TLBO is a population-based algorithm [34]. It operates on the principle that students learn and improve their performance in a classroom setting. Unlike gradient-based methods, which rely on gradients and can struggle with complex or nonsmooth problems, TLBO can effectively explore the solution space without needing gradient information, making it better suited for such challenges.
2) TLBO does not require algorithm-specific parameters; only basic ones, such as population size and the maximum number of iterations, need to be set. This simplicity makes it easier to use.
3) TLBO achieves a balance between local search, driven by the teacher phase, and global exploration, facilitated by the learner phase. This balance helps the algorithm avoid getting trapped in local optima and increases the chance of finding the global optimal solution.

A demonstration of the workings of the TLBO-based excitation optimization is presented as follows.

Step 1. Initialization: Initialize the number of class members N_{pop} (population size) and the maximum number of iterations N_{iter}. The class members consist of a teacher (with the highest score) and some students. A smaller value of the objective function indicates a higher score. Establish the objective function to be optimized as

$$\underset{\aleph^{\ddagger}}{\text{minimize}} \quad \boldsymbol{J}_1 = \text{cond}(\boldsymbol{H}_b), \tag{32}$$

where $\aleph^{\ddagger} \in \mathbb{R}^{1\times(2L+3)n_\rho}$ is the set of decision variables for n_ρ joints, with each joint containing $2L+3$ coefficients to be optimized. Initialize the learning method $\boldsymbol{X}_d \in \mathbb{R}^{1\times(2L+3)n_\rho}$ for each member d ($d = 1,\ldots,N_{\text{pop}}$). Vector $\boldsymbol{X}_d$ represents the decision variables, with its pth element quantifying the learning method of member d for subject p. The elements of $\boldsymbol{X}_d$ are arranged into n_ρ groups, with each group corresponding to a set of coefficients for a joint, e.g., q_k, where the first $2L$ elements represent the active decision variables a_i^k and b_i^k ($i = 1,\ldots,L$), and the remaining three elements represent the passive decision variables $q_{k,0}$, $\dot{q}_{k,0}$, and $\ddot{q}_{k,0}$.

Furthermore, update each member's learning method $\boldsymbol{X}_d$ using Algorithm 1 (still following the notation $\boldsymbol{X}_d$) to ensure that the excitation trajectory (11) generated by the elements of $\boldsymbol{X}_d$ satisfies physical constraints. Accordingly, the objective function value f_d ($d = 1,\ldots,N_{\text{pop}}$) is evaluated using the corrected learning method $\boldsymbol{X}_d$.

Step 2. Teacher phase: The member with the minimum value f_d is selected as the teacher, whose learning method is designated as $\boldsymbol{X}_{\text{tch}}$, while the remaining members act as students. If multiple members share the same minimum value, one is randomly chosen to be the teacher. In this phase, the teacher imparts their learning methods to the students, aiming to improve the overall performance of the class.

First, the average learning method of all members is calculated as

$$\boldsymbol{X}_{\text{mean}} = \frac{\sum_{d=1}^{N_{\text{pop}}} \boldsymbol{X}_d}{N_{\text{pop}}}. \tag{33}$$

The teacher's influence on the students is determined by

$$\boldsymbol{D}_{\text{mean}} = \boldsymbol{r}_{i_s} \odot (\boldsymbol{X}_{\text{tch}} - T_F \boldsymbol{X}_{\text{mean}}) \tag{34}$$

where $\boldsymbol{r}_{i_s} \in \mathbb{R}^{1\times(2L+3)n_\rho}$ is a vector associated with each subject in the i_sth iteration step, with elements that are random numbers uniformly distributed over [0,1], T_F is a randomly chosen scalar, either 1 or 2, and the operator $\odot$ denotes the Hadamard product. For two matrices $\boldsymbol{A} = (a_{ij})$ and $\boldsymbol{B} = (b_{ij})$ of the same dimension, their Hadamard product $\boldsymbol{A} \odot \boldsymbol{B}$ is $\boldsymbol{C} = (c_{ij})$, where $c_{ij} = a_{ij}b_{ij}$.

Member d ($d = 1,\ldots,N_{\text{pop}}$) updates their potential learning method $\boldsymbol{X}_{d,\text{new}}$ based on the teaching influence $\boldsymbol{D}_{\text{mean}}$ as

$$\boldsymbol{X}_{d,\text{new}} = \boldsymbol{X}_d + \boldsymbol{D}_{\text{mean}}. \tag{35}$$

Next, the potential learning method $\boldsymbol{X}_{d,\text{new}}$ is corrected via Algorithm 1 (still following the notation $\boldsymbol{X}_{d,\text{new}}$), ensuring that the excitation trajectory (11) generated by the elements of $\boldsymbol{X}_{d,\text{new}}$ satisfies all physical constraints. The objective function value $f_{d,\text{new}}$ is then evaluated based on the corrected $\boldsymbol{X}_{d,\text{new}}$.

If $f_{d,\text{new}}$ is smaller than f_d, member d accepts $\boldsymbol{X}_{d,\text{new}}$ as their new learning method, thus

$$\boldsymbol{X}_d \leftarrow \boldsymbol{X}_{d,\text{new}}, \quad \boldsymbol{f}_d \leftarrow \boldsymbol{f}_{d,\text{new}}. \tag{36}$$

Otherwise, the original learning method $\boldsymbol{X}_d$ is retained.

Step 3. Learner phase: Following the teacher phase, the learner phase commences, where class members exchange and discuss their knowledge. For instance, member d ($d = 1,\ldots,N_{\text{pop}}$) randomly selects another member s ($s \neq d$) to engage in discussion, forming a potential learning method $\boldsymbol{X}_{d,\text{new}}$ defined as

$$\begin{cases} \boldsymbol{X}_{d,\text{new}} = \boldsymbol{X}_d + \boldsymbol{r}_d \odot (\boldsymbol{X}_s - \boldsymbol{X}_d), & f_d > f_s \\ \boldsymbol{X}_{d,\text{new}} = \boldsymbol{X}_d + \boldsymbol{r}_d \odot (\boldsymbol{X}_d - \boldsymbol{X}_s), & f_d \leq f_s. \end{cases} \tag{37}$$

$\boldsymbol{r}_d \in \mathbb{R}^{1\times(2L+3)n_\rho}$ is a vector associated with member d, with elements drawn from a uniform distribution over the interval [0,1]. $\boldsymbol{X}_{d,\text{new}}$ is then corrected via Algorithm 1 (still denoted as $\boldsymbol{X}_{d,\text{new}}$), allowing $f_{d,\text{new}}$ to be evaluated accordingly.

If $f_{d,\text{new}}$ is smaller than f_d, it indicates that member d can achieve a higher score by using $\boldsymbol{X}_{d,\text{new}}$ as their new learning method; thus, member d accepts $\boldsymbol{X}_{d,\text{new}}$ and $\boldsymbol{f}_{d,\text{new}}$ with (36). Otherwise, the original learning method $\boldsymbol{X}_d$ is retained.

Step 4 Termination criterion: Once all members have completed the learner phase, update the iteration step to

$$i_s \leftarrow i_s + 1. \tag{38}$$

If $i_s \leq N_{\text{iter}}$, return to step 2 for a new round of "teacher & learner;" otherwise, the termination condition is satisfied. The member with the smallest objective function value is then selected as the teacher, and their decision variables represent the optimal coefficients for the excitation trajectory.

Remark 3: The TLBO-based excitation optimization, which addresses physical constraints using the analytical approach, is summarized in Fig. 2. Algorithm 1 effectively ensures that all candidate solutions are feasible, thereby promoting the efficiency of the optimization process. In addition, it is worth noting that our analytical approach is versatile and can also be applied to other heuristic or gradient-based optimization algorithms.

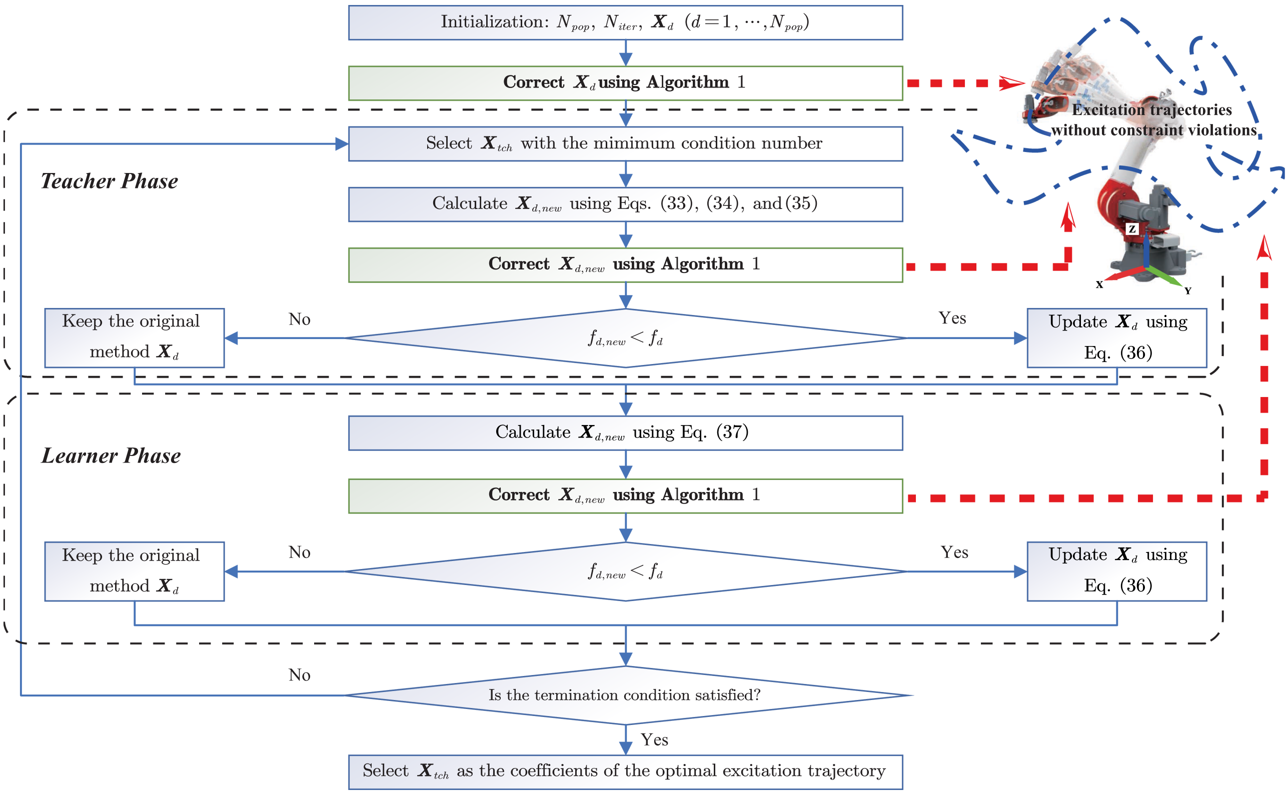

Fig. 2. Flowchart for TLBO-based excitation optimization with the analytical constraint-handling method; the red dashed line illustrates a generated feasible excitation trajectory.

V. Experimental Validation

Our experimental validation is organized into three aspects. The first two parts focus on solving the excitation optimization problem for the robot body model and the payload model, respectively, with particular attention to three metrics: 1) time consumption; 2) constraint violations; and 3) condition numbers. The third part demonstrates the effectiveness of our method in model identification and related applications.

The IP and SQP algorithms serve as the two baseline optimization solvers for comparison in this section, given their widespread use for excitation optimization. These optimization solvers, in conjunction with the optimization problems outlined in Section II, give rise to various excitation optimization methods for evaluation, including the following.

1) Our method
2) *Method A_1:* Problem 1 + the SQP solver.
3) *Method A_2:* Problem 1 + the IP solver.
4) *Method B_1:* Problem 2 + the SQP solver.
5) *Method B_2:* Problem 2 + the IP solver.
6) *Method C_1:* Problem 3 + the SQP solver.
7) *Method C_2:* Problem 3 + the IP solver.

Furthermore, we also evaluated the supervised learning-based excitation optimization method suggested by Duan et al. [32] in the second part, as machine learning methods are regarded as a potential solution to the time-consuming challenge in excitation optimization for payload identification tasks. In addition, a broader comparison of other optimization algorithms[3] for excitation optimization is provided in the supplementary material. The excitation trajectories in these methods were parameterized using a four-term Fourier series, i.e., $L = 4$ and $\omega_f = 2\pi/6$. Data points along the excitation trajectory were recorded in the observation matrix $\boldsymbol{H}_b$ at 8 ms (abbreviated as "ms") intervals, resulting in 750 discrete time instants per cycle.

The performance evaluation took place on a personal computer configured as follows: Processor: Intel(R) Core (TM) i5-7200 U CPU @ 2.50 GHz 2.70 GHz, Available memory: 7.87 GB. Both SQP and IP algorithms were executed using the fmincon function from the MATLAB Optimization Toolbox, with the SQP and IP options, respectively. In contrast, our method, including Algorithm 1 and the TLBO solver, was developed using custom MATLAB scripts. The timing tool is the Profiler.[4]

An important consideration is to reevaluate the condition number of the observation matrix associated with the excitation trajectories generated by Methods C_1 and C_2, as their objective functions are grounded in the Hadamard's inequality.

A. Excitation Optimization for the Robot Body Model

This subsection evaluates the excitation optimization for a 6 DOF robot body model (HSR-CO605: 5-kg payload capacity,

[3] Including sequential least squares programming, PSO, and others.
[4] [Online]. Available: https://www.mathworks.com/help/matlab/ref/profile.html

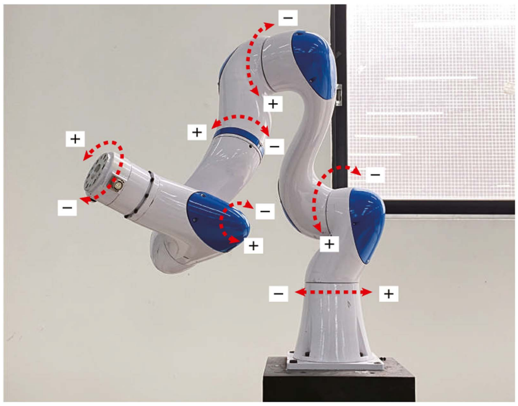

Fig. 3. HSR - CO605: a 6 degree-of-freedom robot.

TABLE I
BOUNDS ON POSITION, VELOCITY, AND ACCELERATION FOR THE HSR-CO605 ROBOT JOINTS

Item	Pos. (Unit: $^\circ$)	Vel. (Unit: $^\circ/s$)	Acc. (Unit: $^\circ/s^2$)
Joint 1	$[-160,\ +160]$	$[-110,\ +110]$	$[-380,\ +380]$
Joint 2	$[-160,\ -30]$	$[-110,\ +110]$	$[-380,\ +380]$
Joint 3	$[-20,\ +220]$	$[-230,\ +230]$	$[-780,\ +780]$
Joint 4	$[-170,\ +170]$	$[-230,\ +230]$	$[-780,\ +780]$
Joint 5	$[-115,\ +115]$	$[-230,\ +230]$	$[-780,\ +780]$
Joint 6	$[-170,\ +170]$	$[-230,\ +230]$	$[-780,\ +780]$

* The listed bounds for joint positions are set based on experimental needs and do not represent the mechanical limits.

25-kg weight, 30-μm repeatability), as shown in Fig. 3. The bounds on position, velocity, and acceleration (abbreviated as Pos., Vel., and Acc.) for all joints are listed in Table I.

Several factors, including the underlying principles of the optimization algorithm, the objective function, the constraints, and the code quality, would influence the evaluation of time consumption. Objectively, the execution of the MATLAB Optimization Toolbox is more efficient than the self-written TLBO scripts, typically avoiding redundant computational steps. For a fair analysis, this experiment evaluates the time consumption of the aforementioned methods from two aspects as follows.

1) *Module Cost:* The execution time of key modules, including the objective function via the condition number or the Hadamard's inequality, the model $\boldsymbol{W}_b \in \mathbb{R}^{6\times 52}$, and the observation matrix $\boldsymbol{H}_b \in \mathbb{R}^{4500\times 52}$.
2) *Optimization Cost:* The total time consumption to accomplish the task of generating optimal excitation trajectories under specific technical specifications.

The specifications for the TLBO algorithm refer to: the maximum number of iterations N_{iter}, the population size N_{pop}, the initialization ranges of decision variables, the objective function, etc.; for the SQP and IP solver, the specifications refer to: "MaxFunctionEvaluations" (maximum number of function evaluations allowed), "MaxIterations" (maximum number of iterations allowed), "ConstraintTolerance" (tolerance on the constraint violations), "StepTolerance" (termination tolerance on decision variables), the objective function, and the initialization ranges of decision variables, etc.

TABLE II
TIME CONSUMPTION TESTS OF THE MODULE COST VIA THE MATLAB PROFILER (UNIT: MS)

Item	$\boldsymbol{W}_b \in \mathbb{R}^{6\times 52}$	$\boldsymbol{H}_b \in \mathbb{R}^{4500\times 52}$	$\boldsymbol{J}_1$	$\boldsymbol{J}_2$
Module cost	0.625	468.495	8.385	2.305

* Part A of the supplementary material has a log of the execution time.

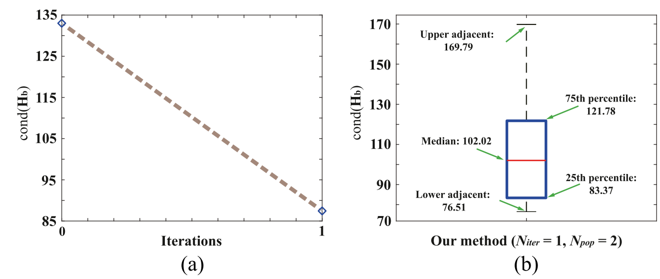

Fig. 4. Condition number of $\boldsymbol{H}_b$ associated with the excitation trajectories generated by our method. (a) Convergence plot of the condition number during a specific run of optimization. (b) Boxplot shows how the condition numbers are distributed of 30 independent runs of our method.

Regardless of the method chosen, the model $\boldsymbol{W}_b$, the observation matrix $\boldsymbol{H}_b$, and the objective functions ($\boldsymbol{J}_1$ and $\boldsymbol{J}_2$) are all developed using custom scripts. Consequently, the module cost is entirely independent of the differences between toolbox and nontoolbox programs. In contrast, the optimization cost is influenced by the quality of the available code.

Table II lists the time consumption of several typical modules. It is evident that the execution time of $\boldsymbol{J}_2$ is less than one-third that of $\boldsymbol{J}_1$, indicating an improvement in computational efficiency attributed to the Hadamard's inequality. However, compared to the computational cost of $\boldsymbol{H}_b$, the time consumption of either $\boldsymbol{J}_1$ or $\boldsymbol{J}_2$ is relatively minor. The Hadamard's inequality provides limited enhancement in the efficiency of generating optimal excitation trajectories.

1) Single-Step Iteration: We examined an extreme scenario involving evaluation using a single-step iteration. The parameter settings for our method were as follows: $N_{\text{iter}} = 1$, $N_{\text{pop}} = 2$, with the initialization ranges of decision variables set to $[-3, 3]$. Fig. 4(a) plots the convergence curve of the condition number of $\boldsymbol{H}_b$ during a specific run of the optimization process. As shown, the condition number of $\boldsymbol{H}_b$ reaches 87.45 within just one iteration. For practical applications in robot dynamic identification, a condition number converging to 100 or below is generally considered acceptable [24]. In addition, the value of the objective function, 133.01, is obtained at the beginning, representing the contribution made by the "teacher" at the start of the first cycle. Our method completed this run in just 6 s (abbreviated as "s"). Furthermore, our method was independently run 30 times under the same settings. The results are summarized in a boxplot, as shown in Fig. 4(b).

The TLBO-based flowchart (see Fig. 2) illustrates that our method evaluates the objective function six times per cycle using the aforementioned settings. Consequently, the maximum

TABLE III
EVALUATION RESULTS OF EXCITATION OPTIMIZATION WITH SINGLE-STEP ITERATION

Item	Method						
	Our	A_1	A_2	B_1	B_2	C_1	C_2
succ.rate	100%	0%	0%	0%	0%	0%	0%
func.eval	6	55	55	49	49	55	55
opti.cost	7	49	49	47	45	48	48
cond.num	169.79	515.86	451.46	949.32	1335.87	574.24	515.82

[1] "succ.rate" denotes the success rate, representing the percentage of results that satisfy physical constraints in 30 independent runs.
[2] "func.eval" denotes the number of function evaluations.
[3] "opti.cost" and "cond.num" refer to the maximum optimization cost (unit: s) and the maximum condition number in the results of 30 independent runs, respectively.

TABLE IV
CHARACTERISTIC INDEXES OF THE EXCITATION TRAJECTORIES GENERATED BY OUR METHOD

Item		Joint 1	Joint 2	Joint 3	Joint 4	Joint 5	Joint 6
Pos. (°)	UM	97.35	2.45	25.91	42.09	0.00	56.65
	LM	97.35	2.45	25.91	42.09	0.00	56.65
Vel. ($^\circ/s$)	$\dot{q}(0)$	0.00	0.00	0.00	0.00	0.00	0.00
	UM	0.00	20.76	0.00	35.65	98.23	0.00
	LM	46.67	0.00	68.11	0.00	85.29	90.95
Acc. ($^\circ/s^2$)	$\ddot{q}(0)$	0.00	0.00	0.00	0.00	0.00	0.00
	UM	240.74	206.42	285.06	381.08	481.37	338.26
	LM	208.38	224.39	351.59	429.46	425.02	431.96

TABLE V
CHARACTERISTIC INDEXES OF THE EXCITATION TRAJECTORIES GENERATED BY METHOD A_1

Item		Joint 1	Joint 2	Joint 3	Joint 4	Joint 5	Joint 6
Pos. (°)	UM	-164.79	-330.94	76.09	-202.41	-45.36	2.51
	LM	108.99	79.43	-255.90	-55.03	-54.76	-229.32
Vel. ($^\circ/s$)	$\dot{q}(0)$	393.77	160.20	213.35	-178.09	50.99	-149.19
	UM	-369.07	-208.58	-85.79	-219.81	-98.82	-148.12
	LM	-161.49	-415.50	-322.49	-165.56	-98.08	-166.21
Acc. ($^\circ/s^2$)	$\ddot{q}(0)$	735.52	267.17	-414.99	-671.8	-385.34	1041.91
	UM	-652.18	-1020.23	-608.70	-649.57	-66.92	-358.54
	LM	-779.88	-726.59	-252.09	-463.76	126.41	-84.27

number of function evaluations allowed by other methods[5] was also set to 6. Specifically, the "MaxFunctionEvaluations" option in fmincon was set to 6. It is worth noting that, due to the implementation principles of the Optimization Toolbox, the actual number of function evaluations may exceed the set value of "MaxFunctionEvaluations".[6] The initialization ranges of the decision variables for the other methods matched those of our method, and the remaining parameters in fmincon were kept at their default values.

Methods A_1, A_2, B_1, B_2, C_1, and C_2 were independently executed 30 times, with the results summarized in Table III. The maximum optimization cost for our method is only 7 s, while the other methods require nearly 50 s. In these 30 independent runs, our method achieves a maximum condition number of 169.79, which is significantly lower than those obtained by the other methods. Furthermore, Methods B_1 and B_2 demonstrate shorter execution times compared to Methods A_1, A_2, C_1, and C_2. This advantage can be attributed to the fewer decision variables in Methods B_1 and B_2, resulting in fewer function evaluations at the end of the iteration. In addition, the absence of equality constraints simplifies the excitation optimization problem.

Fig. 5 shows the excitation trajectories of six joints generated by our method, representing one of the results from 30 independent runs. In addition, two characteristic indexes are defined to quantitatively assess constraint violations (applicable to position, velocity, and acceleration trajectories):

1) *Upper Margin (UM):* The upper bound minus the maximum value of the trajectory. A positive UM means that the (Pos., Vel., or Acc.) trajectory does not violate its corresponding upper bound.
2) *Lower Margin (LM):* The minimum value of the trajectory minus the lower bound. A positive LM means that the (Pos., Vel., or Acc.) trajectory does not violate its corresponding lower bound.

The characteristic indexes related to Fig. 5 are summarized in Table IV. It can be observed that the position, velocity, and acceleration trajectories of all joints remain within physical constraints. Each joint consistently has at least one motion component that precisely reaches its corresponding bounds, i.e., UM or LM equals zero; therefore, our method improves the coverage of the trajectory space, which has a positive effect on the generalization performance of parameter identification. In addition, the velocity and acceleration of all joints start from zero. Notably, the symmetry of the UM and LM values for the position trajectories in Table IV results from the central-translation operation in Algorithm 1.

In contrast, none of the other methods successfully identify feasible solutions that satisfy the physical constraints. The optimization results of Method A_1 (one of the 30 runs) serve as an example. At the end of this run, the maximum constraint violation metric "Feasibility" displayed by the Optimization Toolbox is 1.818×10^1, indicating that the physical constraints have been violated (the default threshold for "Feasibility" to satisfy constraints is 10^{-8}). Fig. 6 illustrates the excitation trajectory of joint 2 generated by Method A_1.

Tables V –X summarize, in turn, the characteristic indexes of constraint violations of the excitation trajectories (derived from one of the results of 30 runs) generated by Methods A_1, A_2, B_1, B_2, C_1, and C_2. It is evident that the Fourier-polynomial hybrid parameterization (Methods B_1 and B_2) can satisfy the initial conditions, but it proves ineffective in meeting the physical limits. All methods involved in the comparison significantly violate the constraints within a single-step iteration. In our experiments, setting "MaxFunctionEvaluations" $= 6$ achieves the effect of limiting the process to a single-step iteration.

[5]To account for differences in algorithm execution, it is more preferable to set maximum function evaluations rather than maximum iterations.

[6]"Iterations and Function Counts" description. [Online]. Available: https://ww2.mathworks.cn/help/releases/R2020a/optim/ug/iterations-and-function-counts.html

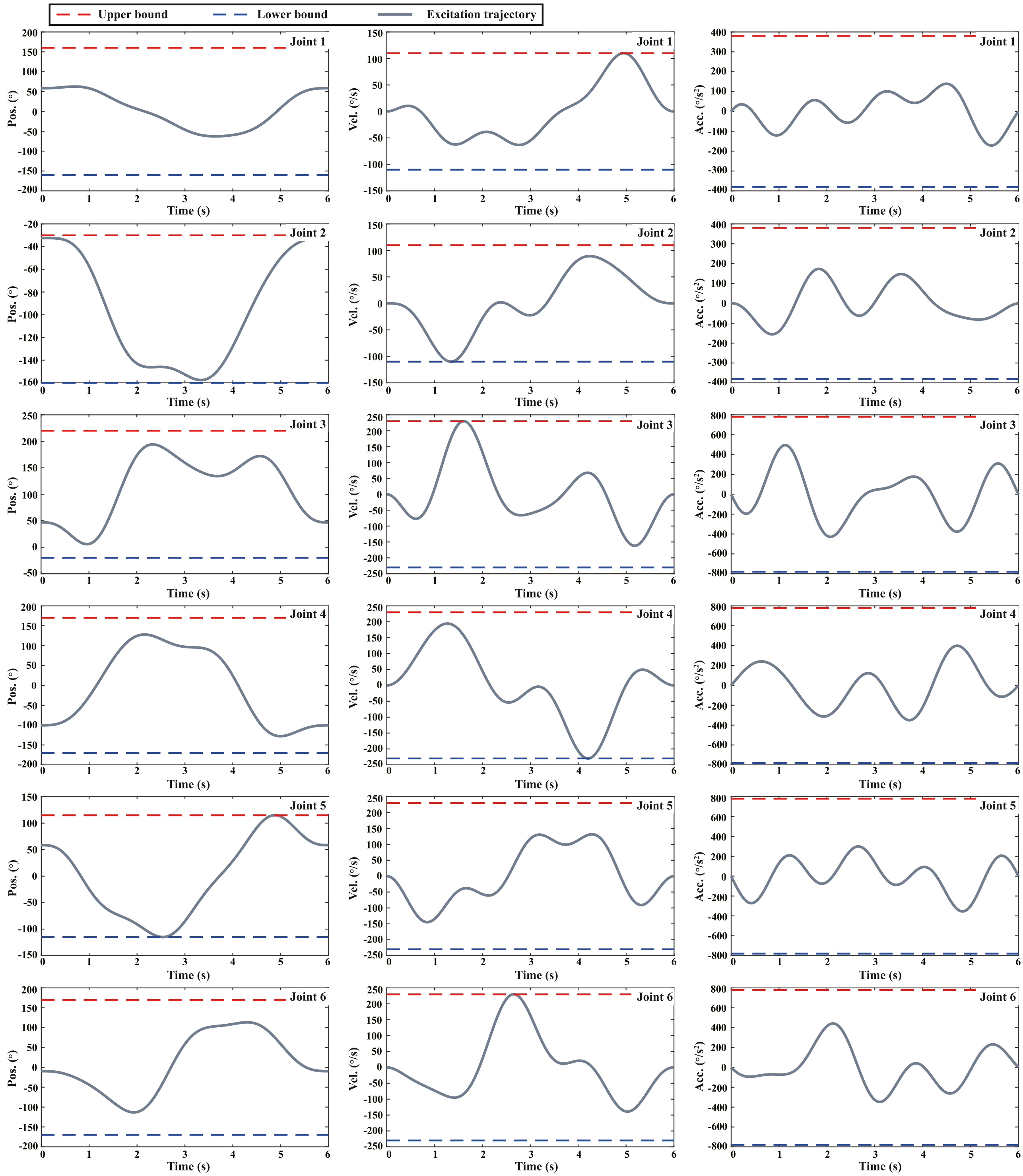

Fig. 5. Excitation trajectories generated by our method ($N_{\text{iter}} = 1$, $N_{\text{pop}} = 2$).

2) Multistep Iterations: The evaluation with a single-step iteration focuses on the methods' performance in handling physical constraints. In this subsection, tests involving multistep iterations were conducted to align with practical applications. The parameter settings for our method were as follows: $N_{\text{iter}} = 10$, $N_{\text{pop}} = 15$, with the initialization ranges of decision variables set to $[-3, 3]$. Fig. 7(a) shows the convergence curve of the condition number of $\boldsymbol{H}_b$ during a specific run, which has an optimization cost of only 205 s and achieves a condition number of 58.22. Furthermore, our method was tested over 20 independent runs, with the results statistically presented in Fig. 7(b). The maximum condition number among these 20 optimization results is as low as 71.08, demonstrating the superior performance of our method.

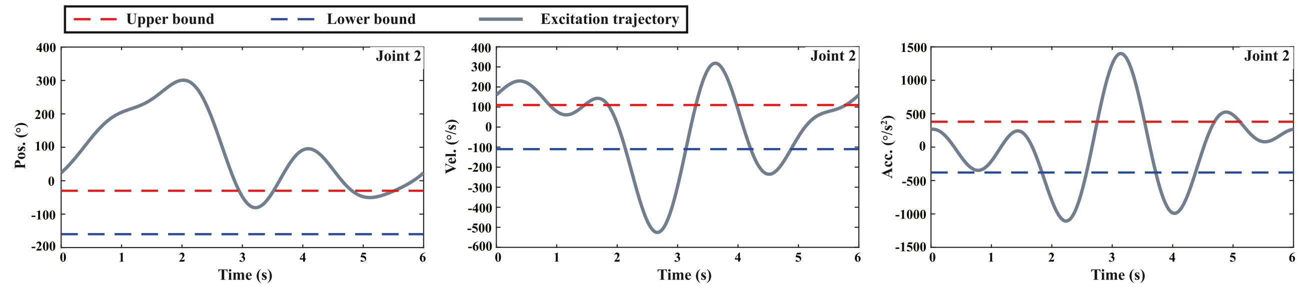

Fig. 6. Excitation trajectories generated by Method A_1 (“MaxFunctionEvaluations” = 6, Joint 2).

TABLE VI
CHARACTERISTIC INDEXES OF THE EXCITATION TRAJECTORIES GENERATED BY METHOD A_2

Item		Joint 1	Joint 2	Joint 3	Joint 4	Joint 5	Joint 6
Pos. (°)	UM	29.58	-237.10	56.51	2.25	-20.63	-85.31
	LM	-114.77	38.78	-308.72	74.69	-182.24	20.91
Vel. ($°/s$)	$\dot{q}(0)$	-220.66	-287.31	-2.92	71.46	324.95	-289.55
	UM	-216.62	-251.68	-230.04	-14.74	-156.16	-248.38
	LM	-252.57	-221.13	-131.21	-46.45	-92.80	-100.39
Acc. ($°/s^2$)	$\ddot{q}(0)$	866.41	-548.19	-113.87	3.14	-693.30	483.14
	UM	-741.45	-459.22	-387.92	-128.38	-406.31	-147.44
	LM	-654.83	-793.48	-558.40	-163.38	-346.65	-283.99

TABLE VII
CHARACTERISTIC INDEXES OF THE EXCITATION TRAJECTORIES GENERATED BY METHOD B_1

Item		Joint 1	Joint 2	Joint 3	Joint 4	Joint 5	Joint 6
Pos. (°)	UM	-444.99	-1261.98	200.12	371.92	-338.63	186.73
	LM	122.37	114.95	-1061.91	-1052.82	174.56	-225.26
Vel. ($°/s$)	$\dot{q}(0)$	0.00	0.00	0.00	0.00	0.00	0.00
	UM	-276.12	-750.41	-817.45	-514.18	-75.54	-161.45
	LM	-387.91	-995.88	-287.82	-538.65	-150.84	-157.78
Acc. ($°/s^2$)	$\ddot{q}(0)$	0.00	0.00	0.00	0.00	0.00	0.00
	UM	-350.58	-1501.70	-827.04	-436.19	-6.17	135.93
	LM	-227.60	-938.37	-865.44	-681.83	-290.17	29.67

TABLE VIII
CHARACTERISTIC INDEXES OF THE EXCITATION TRAJECTORIES GENERATED BY METHOD B_2

Item		Joint 1	Joint 2	Joint 3	Joint 4	Joint 5	Joint 6
Pos. (°)	UM	11.87	-98.59	153.92	-526.47	347.85	207.24
	LM	83.97	-403.03	-689.50	237.15	-1106.68	-483.11
Vel. ($°/s$)	$\dot{q}(0)$	0.00	0.00	0.00	0.00	0.00	0.00
	UM	-117.55	-544.44	-342.56	-346.98	-341.00	-255.42
	LM	-185.32	-250.98	-251.23	-159.17	-640.10	-126.95
Acc. ($°/s^2$)	$\ddot{q}(0)$	0.00	0.00	0.00	0.00	0.00	0.00
	UM	-487.20	-815.94	-14.71	-131.60	-311.79	-219.71
	LM	-204.86	-645.07	63.93	-188.39	-509.86	91.24

TABLE IX
CHARACTERISTIC INDEXES OF THE EXCITATION TRAJECTORIES GENERATED BY METHOD C_1

Item		Joint 1	Joint 2	Joint 3	Joint 4	Joint 5	Joint 6
Pos. (°)	UM	-64.69	-94.36	-13.48	-15.16	-139.74	-32.62
	LM	42.04	-145.34	-136.19	18.63	27.90	32.90
Vel. ($°/s$)	$\dot{q}(0)$	-371.19	-75.31	171.72	-248.45	159.94	327.26
	UM	-226.77	-350.90	-103.20	-138.86	-204.05	-115.23
	LM	-290.02	-238.40	-140.75	-35.62	-63.46	-160.89
Acc. ($°/s^2$)	$\ddot{q}(0)$	-472.38	-598.59	-316.85	-6.58	664.88	-313.99
	UM	-488.88	-549.13	58.07	-257.49	-341.30	201.15
	LM	-871.43	-575.18	-348.45	-199.39	-459.04	-304.61

TABLE X
CHARACTERISTIC INEXCES OF THE EXCITATION TRAJECTORIES GENERATED BY METHOD C_2

Item		Joint 1	Joint 2	Joint 3	Joint 4	Joint 5	Joint 6
Pos. (°)	UM	-161.05	-366.32	-127.18	174.45	-200.87	24.69
	LM	66.94	61.88	-88.96	-196.72	-65.31	-107.60
Vel. ($°/s$)	$\dot{q}(0)$	-184.22	99.55	142.77	339.23	256.61	354.23
	UM	-428.28	-229.34	-177.03	-273.41	-26.85	-243.95
	LM	-191.08	-171.58	-240.38	-34.79	-133.10	-306.50
Acc. ($°/s^2$)	$\ddot{q}(0)$	-167.21	139.76	-917.51	-1050.86	-20.24	-834.36
	UM	-839.09	-430.99	-580.13	-470.06	84.69	-857.78
	LM	-700.32	-481.00	-724.79	-430.77	10.98	-456.06

Furthermore, the compared methods were also evaluated using multistep iterations, with “MaxFunctionEvaluations” set to 4200 (insufficient iterations hinder achieving desired optimization goals, while excessive iterations consume a considerable amount of execution time). Similarly, all methods were independently run 20 times, with their results summarized in Table XI.

It is worth emphasizing that only our method achieves a 100% success rate, meaning that every run generates excitation trajectories that satisfy physical constraints. In contrast, other methods struggle to achieve even a 90% success rate, so no boxplots are provided for their results. In addition, the condition numbers obtained by our method are both excellent and highly consistent. Method A_2 is also comparable to our method in terms of the condition number. Another noteworthy aspect is the optimization cost: the compared methods require approximately half an hour to complete the 4200 function evaluations (similar execution times are documented in Han’s research [24]). In contrast, our method takes less than 4 min, representing a significant improvement.

Our method requires setting very few parameters, needing only the maximum number of iterations, the population size,

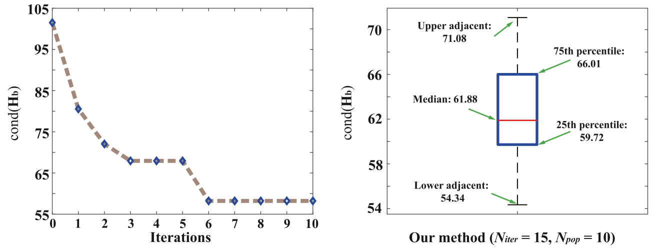

(a) (b)

Fig. 7. Condition number of $\boldsymbol{H}_b$ associated with the excitation trajectories generated by our method. (a) Convergence plot of the condition number during a specific run of optimization. (b) Boxplot shows how the condition numbers are distributed of 20 independent runs of our method.

TABLE XI
EVALUATION RESULTS OF EXCITATION OPTIMIZATION WITH MULTISTEP ITERATIONS

Item	Method						
	Our	A_1	A_2	B_1	B_2	C_1	C_2
succ.rate	100%	80%	65%	25%	55%	85%	55%
opti.cost	224	2172	2189	1896	1811	1937	1952
max.cond	71.08	176.74	77.29	214.04	196.01	220.44	1.6×10^6
min.cond	54.34	107.37	54.77	73.98	110.39	73.59	243.83

[1] "succ.rate" denotes the success rate, representing the percentage of results that satisfy physical constraints in 20 independent runs.
[2] "opti.cost" refers to the maximum optimization cost (unit: s) recorded during the 20 independent runs.
[3] "max.cond" and "min.cond" indicate the maximum and minimum condition numbers, respectively, among the results that meet physical constraints in the 20 independent runs.
[4] The maximum condition number for Method C_2 is excessively large, rendering its precise value less significant.

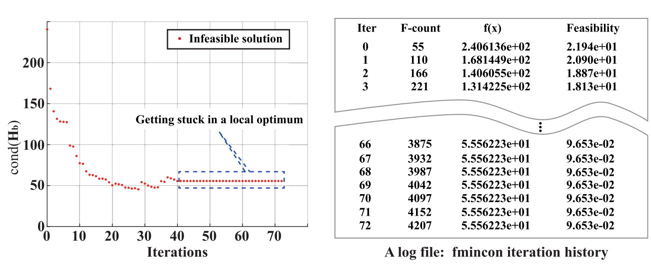

Iter	F-count	f(x)	Feasibility
0	55	2.406136e+02	2.194e+01
1	110	1.681449e+02	2.090e+01
2	166	1.406055e+02	1.887e+01
3	221	1.314225e+02	1.813e+01
⋮			
66	3875	5.556223e+01	9.653e-02
67	3932	5.556223e+01	9.653e-02
68	3987	5.556223e+01	9.653e-02
69	4042	5.556223e+01	9.653e-02
70	4097	5.556223e+01	9.653e-02
71	4152	5.556223e+01	9.653e-02
72	4207	5.556223e+01	9.653e-02

(a) (b)

Fig. 8. Specific run of Method A_2. (a) Convergence plot of the condition number of $\boldsymbol{H}_b$ during this search process. (b) Log file of the iteration display. "F-count": number of function evaluations, "Iter": iterations, "f(x)": objective function value; "Feasibility": maximum constraint violation [44]; "$me \pm n$": "$m \times 10^{\pm n}$".

and the initialization ranges of decision variables. Notably, these settings do not affect the optimization success rate, which remains at 100%. In other words, our method consistently finds feasible excitation trajectories that satisfy physical constraints, regardless of the parameter settings. Compared to our method, the other examined methods reveal several common shortcomings, which are illustrated through individual case analyses.

- *Deficiency 1:* Getting stuck in a local optimum, and thus, unable to find feasible excitation trajectories.

A specific run of Method A_2 is employed as a case study, with the initialization ranges of decision variables set to $[-3, 3]$. Fig. 8 presents the optimization result alongside a log file detailing the

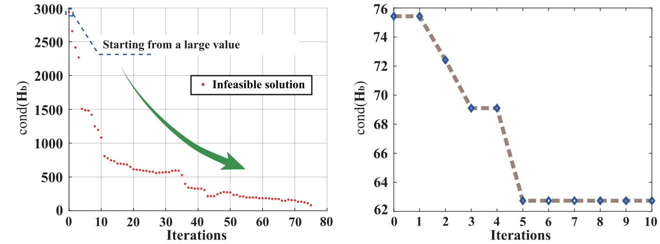

(a) (b)

Fig. 9. Convergence plots of the condition number for the initialization ranges $[-10, 10]$ of decision variables. (a) Method A_2. (b) Our method.

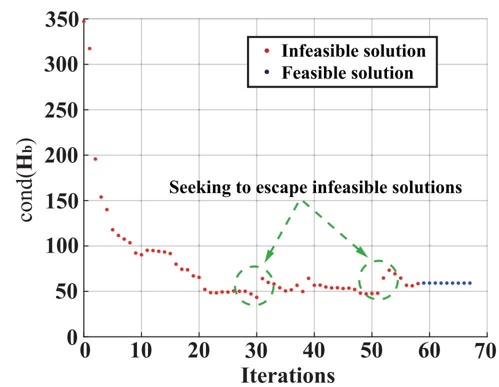

Fig. 10. Convergence curve of the condition number of $\boldsymbol{H}_b$ during a specific run of Method A_2.

iterations. It is evident that this search process gets stuck in a local optimum, having remained in this state since the 41st iteration. Consequently, the subsequent 31 iterations failed to escape this local solution, resulting in no feasible solution that meets the physical constraints being identified. The optimization cost for this run is 1849 s.

- *Deficiency 2:* Determining appropriate solver parameters is challenging and significantly affects the search for the optimal excitation trajectory.

A critical issue is the selection of initialization ranges or initial guesses of the decision variables. Fig. 9(a) shows the convergence plot of Method A_2 with the initialization ranges $[-10, 10]$ of its decision variables. Notably, compared to the parameter settings in Figs. 8(a) and 10, the initialization range of decision variables in Fig. 9(a) is over three times larger (changed from $[-3, 3]$ to $[-10, 10]$); however, the objective function value at the start of the iteration is nearly ten times greater than theirs. Changed the initialization ranges of decision variables of our method from $[-3, 3]$ to $[-10, 10]$, while keeping the other settings unchanged ($N_{\text{iter}} = 10$, $N_{\text{pop}} = 15$). The convergence result during a specific run is shown in Fig. 9(b). A comparison with Fig. 7 reveals that our method is not sensitive to the initial guesses of decision variables.

Expanding the initialization range increases the chances of finding a globally optimal solution. Conversely, we cannot assert that initialization ranges near zero are less likely to generate excitation trajectories that violate physical constraints, since

TABLE XII
FREQUENCY COMPONENTS IN THE VELOCITY TRAJECTORY OF JOINT 1

Item	Amplitudes of major frequency components (Unit: $^\circ/s$)						
	$0f_\omega$	$1f_\omega$	$2f_\omega$	$3f_\omega$	$4f_\omega$	$5f_\omega$	$6f_\omega$
Our method	–	70.5542	21.7787	26.3216	9.2370	–	–
Method B_1	–	32.3001	22.5985	36.0536	20.0206	0.8901	0.5137

[1] f_ω is the fundamental frequency of the excitation trajectory.
[2] The symbol "−" is equivalent to 0.0000 and also indicates the absence of relevant frequency components.

some robots have allowable ranges of motion that deviate from the zero-degree joint positions.

- *Deficiency 3:* Seeking feasible solutions is costly.

The excitation optimization is widely recognized as a time-consuming problem, primarily due to the difficulty of finding feasible solutions under physical constraints. A specific run of Method A_2 is analyzed as a case study, with its fmincon solver configured as described in Deficiency 1. The running result is shown in Fig. 10. It takes 1967 s, with 87% of this time spent on iterations involving infeasible solutions.

In addition to the aforementioned common shortcomings, Methods B_1 and B_2 introduce unspecified frequency components. The fundamental frequency f_ω of the four-term Fourier series in our experiment is $1/T_f$ Hz, where $T_f = 6$ s. Therefore, the specified frequency components include $0f_\omega, 1f_\omega, 2f_\omega, 3f_\omega$, and $4f_\omega$. We performed a discrete Fourier transform on the excitation trajectories (velocity trajectory of joint 1) generated using our method and Method B_1, respectively. The resulting frequency components are presented in Table XII. It is evident that Method B_1 introduces additional frequency components of $5f_\omega$ and $6f_\omega$ (other frequency components are not listed) compared to our method. Furthermore, while these additional frequency components have small amplitudes, they should not be disregarded, as they can still induce resonance in the mechanical structures.

B. Excitation Optimization for the Payload Model

Payload identification is an on-site task characterized by the following requirements.

1) The workspace is confined, requiring minimal robot motion during the identification process.
2) High efficiency is crucial, necessitating rapid searches for optimal excitation trajectories, ideally within seconds.
3) Reliability is paramount, emphasizing the necessity of consistently generating feasible excitation trajectories.

We compared the performance of our method against Methods A_1, A_2, B_1, B_2, C_1, and C_2 for excitation optimization of the HSR-CO605 robot's payload model, with particular emphasis on the success rate and time consumption.

During the execution of payload identification, joints 1 and 2 were set to remain stationary at positions 82° and -107°, respectively. In addition, the motion of joint 3 was limited to a range between 160°–200°. These settings are specific to the described test, and the allowable range of motion for all joints is detailed in Table XIII. The dynamic model of the payload is $\boldsymbol{W}_b \in \mathbb{R}^{4\times10}$, and its observation matrix is $\boldsymbol{H}_b \in \mathbb{R}^{3000\times10}$. We

TABLE XIII
CASE: ALLOWABLE RANGE OF MOTION FOR ALL JOINTS OF THE HSR-CO605 ROBOT IN A PAYLOAD IDENTIFICATION TASK (UNIT: $^\circ$)

Joint 1	Joint 2	Joint 3	Joint 4	Joint 5	Joint 6
82	-107	$[160, 200]$	$[-170, 170]$	$[-115, 115]$	$[-170, 170]$

[*] Joints 1 and 2 can remain stationary at any angle, while the motion ranges of the other joints can be adjusted according to practical requirements.

TABLE XIV
PERFORMANCE COMPARISON OF EXCITATION OPTIMIZATION FOR THE PAYLOAD MODEL BY LIMITING THE OPTIMIZATION COST

Item	Method						
	Our	A_1	A_2	B_1	B_2	C_1	C_2
(1 s) succ.rate	100%	0%	0%	0%	0%	0%	0%
max.cond	5.11	–	–	–	–	–	–
ave.cond	4.48	–	–	–	–	–	–
(5 s) succ.rate	100%	0%	0%	0%	0%	0%	0%
max.cond	4.51	–	–	–	–	–	–
ave.cond	4.22	–	–	–	–	–	–
(20 s) succ.rate	100%	40%	25%	0%	0%	75%	95%
max.cond	3.99	9.78	4.37	–	–	12.92	23323
ave.cond	3.81	8.10	3.93	–	–	8.06	1640

[1] "succ.rate" stands for the success rate when time consumption is limited to approximately 1, 5, or 10 s. The success rate is the percentage of results that meet physical constraints in 20 independent runs.
[2] "max.cond" indicates the maximum condition number among results that meet physical constraints in 20 independent runs. "ave.cond" is the average condition number of results meeting physical constraints. These values may vary across different test runs due to inherent variability in the optimization process.
[3] The symbol "−" denotes no relevant results.

evaluated each method in implementing excitation optimization within a given time. Specifically, the time consumption were regulated by imposing a constraint on the maximum number of function evaluations. In addition, all methods were run independently 20 times.

Time consumption for completing the excitation optimization task was limited to around 1 s. The parameter settings for our method were as follows: $N_{\text{iter}} = 2$, $N_{\text{pop}} = 6$, with the initialization ranges of decision variables set to $[-3, 3]$. For the other methods, the fmincon solver was configured as follows: "MaxFunctionEvaluations" $= 30$, the initialization ranges of decision variables were $[-3, 3]$. Table XIV presents the evaluation results for all methods. Only the excitation trajectories generated by our method satisfy the physical constraints, while none of the other methods can produce excitation trajectories that meet these constraints within an optimization cost of 1 s. In addition, among the 20 evaluation results of our method, the maximum condition number is only 5.11, indicating a high-quality optimization outcome.

Furthermore, the time consumption for completing the excitation optimization task was limited to around 5 s. To achieve this, we adjusted the parameters N_{pop} and "MaxFunctionEvaluations" to 30 and 140, respectively, while keeping the rest of the parameters unchanged. Table XIV presents the evaluation results for all methods. Notably, the success rate of our method is 100%, indicating that all 20 optimization results meet the physical constraints. In contrast, none of the results from the compared methods meet the physical constraints, leading to a success rate of 0%.

After relaxing the time consumption to around 20 s, all methods except Methods B_1 and B_2 can generate excitation trajectories that meet the physical constraints with some probability. Notably, while Method C_2 achieves a success rate of 95%, its results exhibit a very large condition number, indicating that the observation matrix is ill-conditioned. Method A_2 has a condition number comparable to our method, but its success rate is only 25%.

Overall, in the context of excitation optimization for payload identification, our method outperforms Methods A_1, A_2, B_1, B_2, C_1, and C_2. We also assessed the supervised learning-based excitation optimization approach introduced by Duan et al. [32]. Let $\boldsymbol{q}_{\text{ini}} \in \mathbb{R}^6$ represent the initial joint position of the robot prior to executing the excitation trajectory, with $q_{k,\text{ini}}$ denoting the kth element of $\boldsymbol{q}_{\text{ini}}$. The trajectory was parameterized as described in (1), with $L = 4$. Following the Duan's approach, $q_{k,0}$ was set to $q_{k,\text{ini}}$, imposing additional constraints on the initial conditions as $q_k(0) = q_{k,\text{ini}}$. In this case, a total of eight Fourier coefficients must be determined for each joint. For joints 3 to 6, there are a total of 32 coefficients to be optimized. Within the supervised learning framework, it is assumed that each $\boldsymbol{q}_{\text{ini}}$ is associated with a set of optimal Fourier coefficients.

We randomly generated initial positions within the robot's configuration space and then applied a classical gradient-based optimization method to perform excitation optimization on these positions. Notably, gathering this dataset took nearly 5 days on the computational platform described in the experiments. We used a multilayer perceptron (MLP) neural network[7] as our model, with $\boldsymbol{q}_{\text{ini}}$ as the input and the 32 coefficients as the output. The MLP model included an input layer with six units, followed by two hidden layers with 64 and 32 neurons, respectively, using ReLU activation functions. The output layer, with 32 units, was designed for the regression task. The network was trained using the Adam [45] optimizer, starting with an initial learning rate of 0.001. A piecewise learning rate schedule was applied, halving the learning rate every 100 epochs, with a maximum of 500 epochs. The dataset was split into a training set (2000 samples), a validation set (500 samples), and a test set (500 samples). Both input and output data were standardized by subtracting the mean and dividing by the standard deviation. The loss function was defined as the mean squared error between the predicted coefficients and the target coefficients. The Deep Learning Toolbox in MATLAB was used for implementing the MLP model. Using the trained MLP model, we generated excitation trajectories for the payload model based on 20 selected initial joint positions, with joints 1 and 2 fixed as specified in Table XIII, while joints 3 to 6 were randomly assigned within their allowable ranges. Fig. 11 shows the time consumption and condition numbers of $\boldsymbol{H}_b$ for these tests. Duan et al. proposed a postprocessing procedure aimed at ensuring that the excitation trajectories generated by the machine learning approach satisfy physical constraints, though further details are beyond the scope of this article. Here,

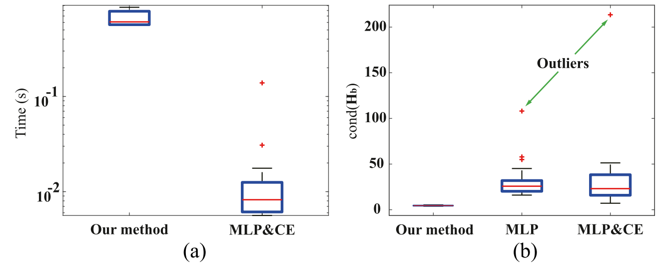

Fig. 11. Comparison of our method ($N_{\text{iter}} = 2$, $N_{\text{pop}} = 6$) with the supervised learning-based approach. (a) Time required for generating excitation trajectories. (b) Condition number of the observation matrix for the payload model.

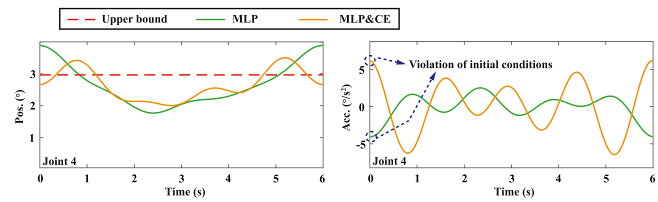

Fig. 12. Constraint-violation of the excitation trajectories generated by MLP and MLP&CE.

we refer to the postprocessed MLP model as "MLP&CE." As expected, MLP&CE shows excellent performance with significantly lower time consumption, which is an order of magnitude lower than the average time of our method. Both our method and the MLP model involve deterministic computational steps, indicating that, in theory, time consumption should remain constant.[8] This advantage is not seen in classical excitation optimization methods, which tend to have unpredictable execution times.

However, the MLP exhibits a deficiency in terms of condition numbers, with values reaching as high as 108, clearly failing to meet the expected level. Furthermore, the postprocessing procedure for constraints exacerbates the condition number, with the maximum value exceeding 200 in the 20 test results. In stark contrast, the condition number distribution generated by our method is tightly clustered, with a maximum value of only 5.11.

The most significant challenge in practical application is the violation of physical constraints by the machine learning approach. As shown in Fig. 12, the excitation trajectories generated by the MLP fail to satisfy the physical constraints. In addition, the postprocessing procedure in MLP&CE is unable to effectively address these constraints. In terms of condition numbers, our experimental results for MLP and MLP&CE are consistent with those reported in [32], where the high condition numbers are attributed to the limited generalization performance of the trained model. Regarding constraint handling, the MLP inherently fails to directly address physical constraints. Furthermore, the constraint-handling method in MLP&CE is a rudimentary solution that is effective only under specific ideal conditions, as noted in [32].

[7]Duan et al. [32] trained individual Gaussian process models for each Fourier coefficient. However, we found this approach to be time-consuming, as detailed in our supplementary material. Moreover, we believe the Fourier coefficients are correlated, making independent training inappropriate.

[8]The fluctuations in execution time presented in Fig. 11 arise from unavoidable practical factors, such as system load from background processes competing for CPU resources and variations in memory management.

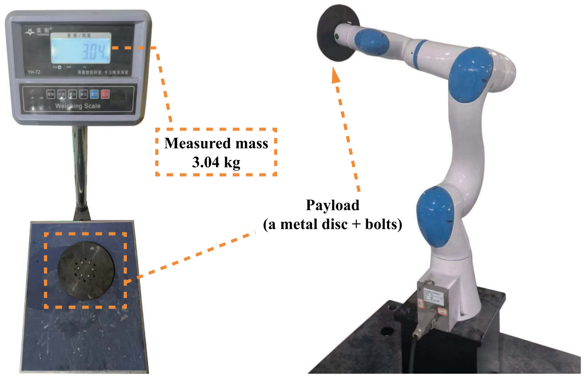

Fig. 13. Platform for payload identification: A robot HSR-CO605, a payload (a metal disc + bolts), an electronic weighing instrument.

C. Identification Results and Application Benefits

In this subsection, we demonstrate the effectiveness of our method in model identification and its applicability to different types of robots.[9] It is worth noting that the robot's links contain various electrical components and mechanisms, which make it challenging to obtain precise reference values for the dynamic parameters of the body model. In light of this, directly evaluating the accuracy of these parameters is not practically feasible. In practice, identifying the dynamic parameters of the payload model relies on a well-established dynamic model of the robot body [46], whereas the payload's mass can be measured with high precision. Therefore, assessing the accuracy of the payload identification results is a straightforward approach, and it also reflects the identification accuracy of the body model. In addition, comparing the differences between the predicted forces/torques from inverse dynamics and the measured values is also a common method for evaluating identification results [39]. The most indirect approach is to assess the performance in model-based applications [40], but the results of this evaluation are more closely aligned with the original intention of dynamic research.

The dynamic identification results for the HSR-CO605 body model are provided in the supplementary material. Furthermore, we tested three configurations to compare the performance of our method with that of a machine learning approach (MLP&CE) in terms of payload identification accuracy using the generated excitation trajectories. A payload was mounted on the end flange of the HSR-CO605, with a measured mass of 3.04 kg, as shown in Fig. 13. To mitigate overfitting in the identification results, a linear matrix inequality approach for parameter estimation [47] was employed. Table XV presents the condition numbers of the payload model and the identified mass. The percentage error of the identified mass using our method remains within 2%, while a result from MLP&CE exceeds 4%; the improved accuracy of our method is somewhat related to its smaller condition numbers. It is important to note that the condition number determines the upper bound of the uncertainty in parameter estimation, rather than having a direct proportional relationship with identification

[9]The generation of excitation trajectories is similar across different robots, so repetitive details are omitted.

TABLE XV
PAYLOAD IDENTIFICATION FOR THE HSR-CO605 ROBOT (MEASURED MASS: 3.04 KG)

Configuration	Our method			MLP&CE		
	cond($\boldsymbol{H}_b$)	Identified	$\%e$	cond($\boldsymbol{H}_b$)	Identified	$\%e$
$\boldsymbol{q}_1$	3.35	2.99 kg	1.64%	6.43	2.92 kg	3.95%
$\boldsymbol{q}_2$	3.27	3.00 kg	1.32%	6.71	3.09 kg	1.64%
$\boldsymbol{q}_3$	5.11	3.05 kg	0.33%	26.32	3.19 kg	4.93%

[1] $\%e = |\text{measured mass} - \text{identified mass}|/\text{measured mass} \times 100\%$.
[2] $\boldsymbol{q}_1 = [0, -90, 180, 0, 0, 0]^{\mathrm{T}}$, $\boldsymbol{q}_2 = [82, -107, 180, 0, 0, 0]^{\mathrm{T}}$ (unit: °), and the motion range of joint 3 to joint 6 is consistent with that in Table XIII.
[3] $\boldsymbol{q}_3 = [45, -60, 90, 0, 0, 0]^{\mathrm{T}}$ (unit: °). The motion range of joint 3 is from 70° to 110°, while the motion range of joint 4 to joint 6 is consistent with that in Table XIII.

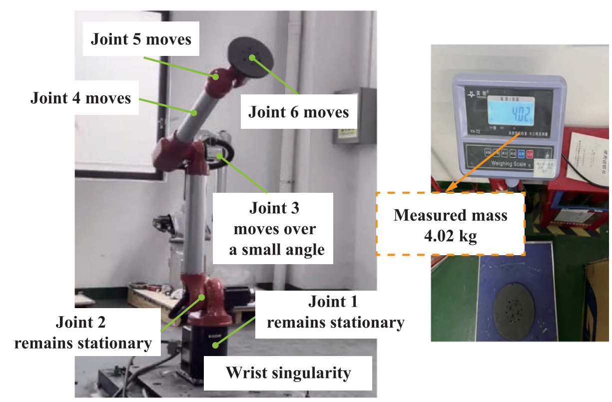

Fig. 14. HSR-BR610 successfully performed payload identification task at a wrist singularity configuration; the measured mass of 4.02 kg is just a case.

accuracy [7]. The remaining parameters of the payload are provided in the supplementary material, but a comparative analysis is not included as the presence of irregular cavities in the payload makes accurate measurements of these parameters difficult.

Furthermore, we conducted a more extensive validation of our method on additional robots. The HSR-BR610 is a 6 DOF robot with a payload capacity of 10 kg, as shown in Fig. 14. Its transmission design differs from that of the HSR-CO605. The HSR-CO605 adopts integrated joint modules [48], typical of collaborative robots, whereas the HSR-BR610's drive train includes bevel gears.

We selected both singular and regular configurations for the HSR-BR610 to conduct payload identification tests with three weight levels: light (3.02 kg), medium (4.02 kg), and heavy (10.04 kg). In addition, these payloads exhibit differences between eccentric and noneccentric characteristics. Payload identification was performed based on our excitation optimization method, with the results summarized in Table XVI. It can be observed that, except for the light payload, the percentage errors of the identified mass for the other payloads are within 2%. Notably, the identification accuracy generally tends to improve as the mass increases. Besides, the identification error for the 3.02-kg payload remains below 3.5%, which still indicates a high level of accuracy.

Furthermore, our method was applied to the HSR-SR201000 robot to generate excitation trajectories, followed by dynamic parameter identification. HSR-SR201000, as shown in Fig. 15, is a 4 DOF selective compliance assembly robot arm (SCARA)

TABLE XVI
PERCENTAGE ERROR STATISTICS OF PAYLOAD IDENTIFICATION ACCURACY FOR THE HSR-BR610 ROBOT

Payload	Configuration	Mass		%e
		Measured	Identified	
eccentric block	regular	3.02 kg	3.12 kg	3.31%
	singular		3.07 kg	1.65%
disc	regular	4.02 kg	4.08 kg	1.49%
	singular		4.03 kg	0.24%
disc	regular	10.04 kg	10.14 kg	0.99%
	singular		10.16 kg	1.19%

[1] $\%e = |\text{measured mass} - \text{identified mass}| / \text{measured mass} \times 100\%$.

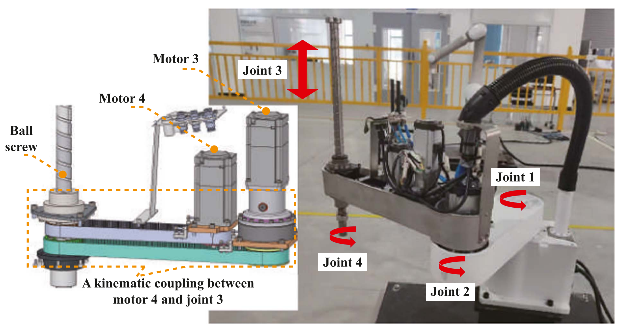

Fig. 15. HSR-SR201000: a SCARA robot with a prismatic joint for joint 3, while the other joints are revolute.

robot, featuring a prismatic joint for joint 3, while the other joints are revolute. Notably, there is kinematic coupling between motor 4 and joint 3, which affects the dynamic behavior as discussed in [49]. We selected a validation trajectory distinct from the identification motion to assess the accuracy of the dynamic model. As shown in Fig. 16, the predicted forces/torques from inverse dynamics closely fit the measured values. Let $\boldsymbol{\tau}_m$ denote the measured force/torque and $\boldsymbol{\tau}_p$ denote the predicted force/torque. The relative force/torque error ϵ_r is given by

$$\epsilon_r = \frac{\|\boldsymbol{\tau}_m - \boldsymbol{\tau}_p\|_2}{\|\boldsymbol{\tau}_m\|_2}. \tag{39}$$

Considering the significant differences in the magnitudes of forces/torques across different joints, using the relative error ϵ_r provides a more objective measure of the prediction accuracy. From the results shown in Fig. 16, it can be observed that the minimum value of ϵ_r is 5.47%, and the maximum value is 8.13%. Based on the statistical analysis of relative force/torque error by Sousa et al. [40], it is evident that our method achieves high-accuracy identification of the model parameters.

Our excitation optimization method was also applied to the HSR-JR6210, a 6 DOF heavy payload robot with a payload capacity of 210 kg, as shown in Fig. 17. Due to its weight of up to 1150 kg, the joint flexibility cannot be ignored, and thus, the robot's state variables are divided into two parts: 1) motor side; and 2) link side. The dynamic behavior of a flexible joint is generally modeled as a two-inertia system [50] connected by a torsional spring and a damper. However, the controller can only directly measure and control the motor side, while the robot's links are driven by joint torsional springs. Therefore, to some

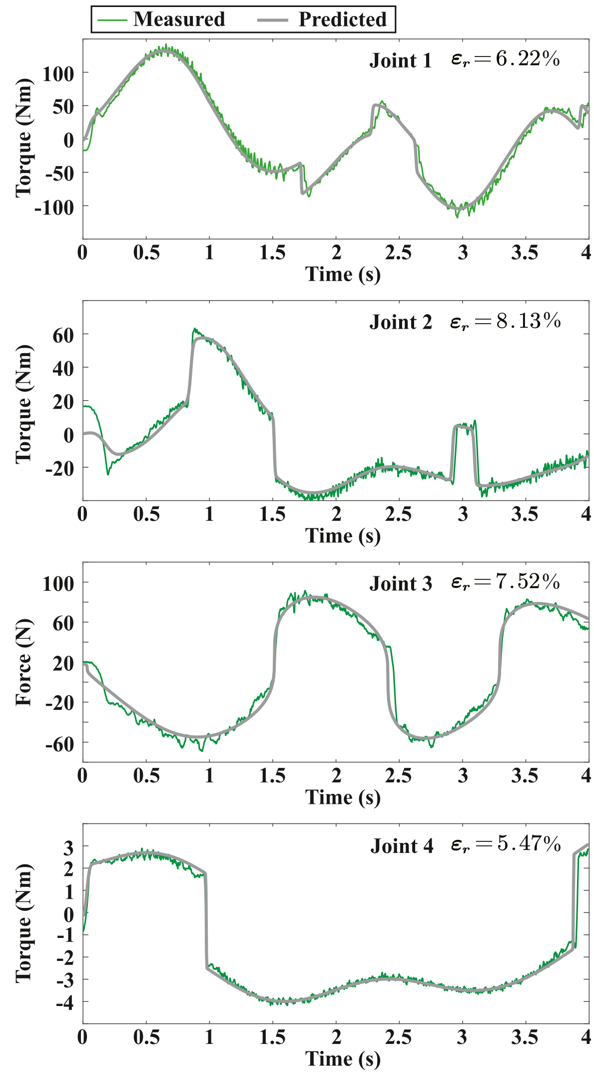

Fig. 16. Comparison between measured and predicted forces/torques for the HSR-SR201000 robot on a validation trajectory; ϵ_r is the relative error.

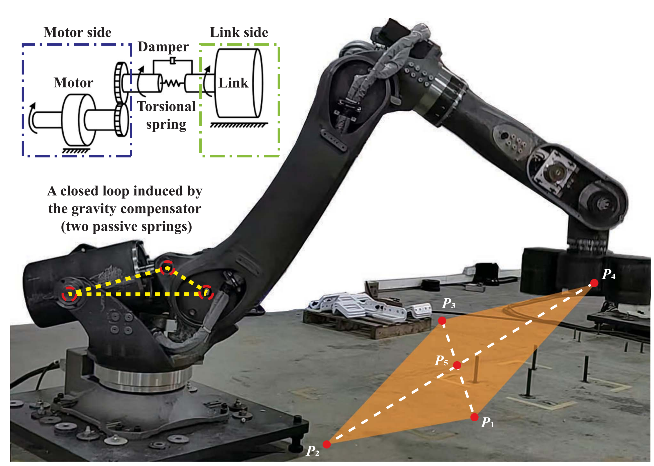

Fig. 17. HSR-JR6210: a 6 DOF heavy payload robot with a 210-kg payload capacity and a gravity compensator. $\boldsymbol{P}_1$:{1500, 500, 580}, $\boldsymbol{P}_2$:{1500, -500, 580}, $\boldsymbol{P}_3$:{2500, -500, 1580}, $\boldsymbol{P}_4$:{2500, 500, 1580}, and $\boldsymbol{P}_5$: {2000, 0, 1080} are five test points defined in the base frame $\mathbb{B}: \{x, y, z\}$ (unit: mm).

TABLE XVII
POSITIONING ERRORS OF A HEAVY PAYLOAD ROBOT BEFORE AND AFTER DEFORMATION ERROR COMPENSATION

Item	Positions				
	$\boldsymbol{P}_1$	$\boldsymbol{P}_2$	$\boldsymbol{P}_3$	$\boldsymbol{P}_4$	$\boldsymbol{P}_5$
e_p (unit: mm)	1.4933	1.4386	4.2371	4.2286	2.6204
e_p^c (unit: mm)	0.2451	0.3085	0.3937	0.3708	0.4109
$(e_p - e_p^c)/e_p \times 100\%$	83.59%	78.56%	90.71%	91.23%	84.32%

[1] e_p and e_p^c are the positioning errors before and after deformation error compensation, respectively.

extent, the heavy payload robot HSR-JR6210 can be considered as an underactuated system [51].

We used a frequency-domain method [52] to identify the motion independent dynamic parameters, such as joint stiffness and motor inertia, in a two-inertia system. Furthermore, considering the high gear ratios and stiffness of industrial robots, the relationship between link-side and motor-side state variables was established, following the principles outlined in [53]. Finally, excitation optimization and parameter identification were carried out for the link-side dynamic model. Evaluating the improvement of positioning accuracy through the deformation error compensation [54] is a straightforward method for verifying the accuracy of the flexible joint dynamic model. Specifically, let $\boldsymbol{q}_d^l \in \mathbb{R}^{6\times 1}$ and $\boldsymbol{\tau}_p^l \in \mathbb{R}^{6\times 1}$ denote the desired joint position and the predicted torque on the link side, respectively, and let $\boldsymbol{K}_s \in \mathbb{R}^{6\times 6}$ be the diagonal joint stiffness matrix. The desired joint position on the motor side $\boldsymbol{q}_d^m \in \mathbb{R}^{6\times 1}$ is corrected as follows:

$$\boldsymbol{q}_d^m = \boldsymbol{q}_d^l + \boldsymbol{K}_s^{-1}\boldsymbol{\tau}_p^l. \tag{40}$$

Five test points were selected within the workspace according to the ISO 9283 standard to compare positioning errors before and after applying deformation error compensation, following the guidelines described in [55]. The results presented in Table XVII indicate that our method remains effective for exciting heavy payload robots with flexible joints.

Finally, we assessed excitation optimization performance by testing the built-in payload identification function in several industry-leading commercial robots. Appendix A presents videos featuring the KUKA LBR iiwa 14 R820 (hereafter referred to as KUKA iiwa) and the ABB IRB 2600 (hereafter referred to as ABB), demonstrating payload identification across three different configurations. However, these robots execute the excitation trajectories uniformly, without optimizing for each specific configuration. Moreover, their excitation trajectories involve single-joint movements rather than multiaxis coordination, which limits their ability to determine the inertia tensor. Identifying the complete dynamic parameters of the payload model is crucial for precise motion control. In addition, as illustrated in Figs. 18 and 19, both the KUKA iiwa and ABB robots have some specific configurations that cannot be identified, as noted in their product manuals. Typically, the KUKA iiwa fails to perform identification in singular configurations, while the ABB robot requires the axis of joint 5 to be horizontally aligned. Given that workspaces are generally narrow and the robots' allowable ranges of motion are fixed once deployed, these

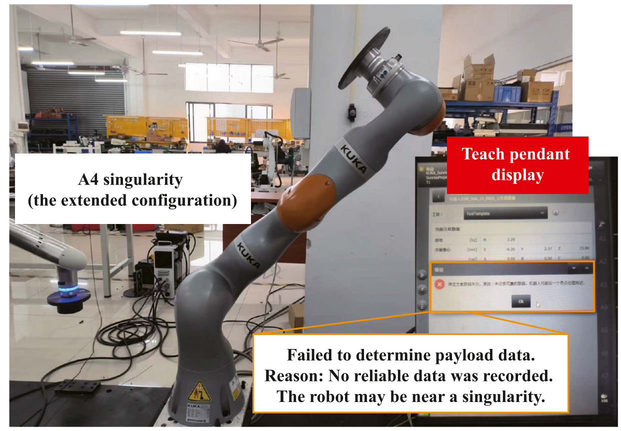

Fig. 18. KUKA iiwa failed to determine payload data at the "A4 singularity" configuration (i.e., the extended configuration).

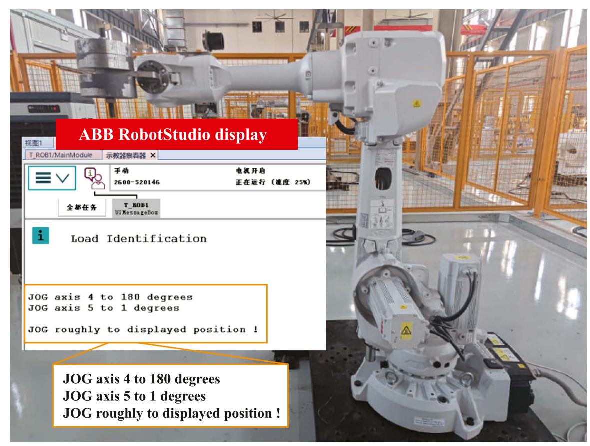

Fig. 19. ABB's joint 5 axis is parallel to the direction of the gravity vector, making it impossible to identify the payload.

limitations hinder effective payload identification. The lack of excitation optimization functionality in these commercial robots for payload identification may stem from two factors: first, the time-consuming aspect of available methods; and second, more importantly, their inability to reliably produce feasible solutions that meet physical constraints. In contrast, our method can quickly and reliably generate an optimal excitation trajectory according to the on-site configuration of the robots.

VI. CONCLUSION

Excitation optimization is an essential step in the dynamic parameter identification of robots, typically formulated as a constrained optimization problem. In existing methods, the solution of excitation optimization relies on heuristic search or iterative methods, which have two common drawbacks: 1) they are time-consuming; and 2) they do not guarantee the discovery of feasible solutions within a limited number of iterations. These challenges hinder the application of excitation optimization in online identification tasks.

In this article, we proposed an analytical approach for handling physical constraints in excitation optimization problems, shifting the search for feasible solutions from an uncertain iterative paradigm to deterministic calculations. This fundamental change ensures that every candidate solution during optimization is feasible. Therefore, our method ensures adherence to physical constraints, achieving a 100% success rate while generating excitation trajectories with small condition numbers within a short time frame (typically in the order of seconds for online tasks related to payload model identification). In fact, our analytical approach can also be used in the dataset collection for machine learning-based excitation optimization methods, helping to reduce time costs. In other words, there is no substantial conflict between these two paradigms.

The experiments included a thorough comparison with existing methods, demonstrating the advantages of our approach in terms of success rates, time efficiency, and condition numbers. Although the tested platforms were limited to collaborative and industrial robots, excitation optimization based on Fourier trajectory parameterization has proven effective for arm model identification in humanoid robots [56] and leg model identification in hexapod robots [57]. Thus, the analytical approach proposed in this article holds potential for broader applicability. However, implementing excitation optimization on these floating-base robots involves additional considerations, such as balance, often requiring a divide-and-conquer strategy for whole-body dynamics.

We would like to clarify the following points. Although the Cartesian space constraints of the robot are more stringent, we do not recommend explicitly considering them in excitation optimization. On one hand, the inclusion of Cartesian constraints significantly increases the optimization burden. On the other hand, the complexities of the real-world environment make strict formalization challenging. A convenient approach is to restrict the allowable joint motion ranges according to the workspace, allowing the robot to perform identification movements slowly before executing excitation trajectories to check for collision risks. Beyond Cartesian constraints, incorporating torque into optimization may become a self-referential problem. Specifically, excitation optimization is inherently intended for parameter identification, and calculating torque relies on model parameters. This issue is particularly pronounced when addressing completely unknown payloads, given the absence of prior model parameters. Generally, limiting the maximum joint velocities and accelerations can effectively meet torque constraints, and motors also have a certain overload capability. Our method is predicated on the assumption that there are no coupled constraints acting collectively on different joints. This premise is applicable to the vast majority of robots but cannot be directly applied to parallelogram arms and parallel robots. In future work, we will explore how to extend the core principles of our analytical approach to overcome this limitation.

Our method has been successfully deployed and validated in the product family of Huashu Robot Company Ltd. Importantly, we have also open-sourced our code on GitHub, allowing researchers to build upon our work and fostering further development within the robotics community.

Appendix A
Videos

Movie 1: Payload identification of an ABB robot at configuration 1. https://youtu.be/gfVudS1STCk

Movie 2: Payload identification of an ABB robot at configuration 2. https://youtu.be/g7BuE1PttMk

Movie 3: Payload identification of an ABB robot at configuration 3. https://youtu.be/3zO4Cop6rJE

Movie 4: Payload identification of a KUKA iiwa robot at configuration 1 (regular). https://youtu.be/W9kgzaSVbNg

Movie 5: Payload identification of a KUKA iiwa robot at configuration 2 (singular). https://youtu.be/AWCemjW69Bg

Movie 6: Payload identification of a KUKA iiwa robot at configuration 3 (regular). https://youtu.be/vNEM5J2FWt0

Appendix B
Codes Available

https://github.com/HuangShifengHUST/AnaAp.PhyConst.ExcitOptimi.DynIDen/tree/master

References

[1] C. Seo, H. Kim, H. Jin, T. Kim, and T. Seo, "Force control of a grinding robotic manipulator with floating base via model prediction optimization control," *IEEE/ASME Trans. Mechatron.*, vol. 28, no. 4, pp. 1911–1919, Aug. 2023.

[2] D. Zurlo, T. Heitmann, M. Morlock, and A. De Luca, "Collision detection and contact point estimation using virtual joint torque sensing applied to a cobot," in *Proc. IEEE Int. Conf. Robot. Automat*., 2023, pp. 7533–7539.

[3] M. Wang, J. Xiao, S. Liu, and H. Liu, "A third-order constrained approximate time-optimal feedrate planning algorithm," *IEEE Trans. Robot.*, vol. 38, no. 4, pp. 2295–2307, Aug. 2022.

[4] P. Mesmer, M. Neubauer, A. Lechler, and A. Verl, "Drive-based vibration damping control for robot machining," *IEEE Robot. Autom. Lett.*, vol. 5, no. 2, pp. 564–571, Apr. 2020.

[5] X. Xiong and A. Ames, "3-D underactuated bipedal walking via H-LIP based gait synthesis and stepping stabilization," *IEEE Trans. Robot.*, vol. 38, no. 4, pp. 2405–2425, Aug. 2022.

[6] J. Vantilt, E. Aertbeliën, F. D. Groote, and J. D. Schutter, "Optimal excitation and identification of the dynamic model of robotic systems with compliant actuators," in *Proc. IEEE Int. Conf. Robot. Automat.*, 2015, pp. 2117–2124.

[7] M. Gautier and W. Khalil, "Exciting trajectories for the identification of base inertial parameters of robots," *Int. J. Robot. Res.*, vol. 11, no. 4, pp. 362–375, 1992.

[8] KUKA LBR iiwa, *Operating and Programming Instructions for System Integrators [KUKA Sunrise.OS 1.11/KUKA Sunrise.Workbench 1.11]*. Augsburg, Germany: KUKA Roboter GmbH, 2016.

[9] *ABB, ROBOTICS Operating manual: IRC5 with FlexPendant [Document ID: 3HAC050941-001, Revision: J]*. Zurich, Switzerland: ABB, 2019.

[10] YASKAWA DX100 Controller, "DX100-configure weight and gravity measure, yaskawa America robotics technical support group," 2018. [Online]. Available: https://www.youtube.com/watch?v=LSY_w-hf6Ps

[11] B. Armstrong, "On finding 'exciting' trajectories for identification experiments involving systems with non-linear dynamics," in *Proc. IEEE Int. Conf. Robot. Automat.*, 1987, pp. 1131–1139.

[12] W. Rackl, R. Lampariello, and G. Hirzinger, "Robot excitation trajectories for dynamic parameter estimation using optimized B-splines," in *Proc. IEEE Int. Conf. Robot. Automat.*, 2012, pp. 2042–2047.

[13] V. Bonnet, P. Fraisse, A. Crosnier, M. Gautier, A. González, and G. Venture, "Optimal exciting dance for identifying inertial parameters of an anthropomorphic structure," *IEEE Trans. Robot.*, vol. 32, no. 4, pp. 823–836, Aug. 2016.

[14] N. Pedrocchi, E. Villagrossi, F. Vicentini, and L. M. Tosatti, "On robot dynamic model identification through sub-workspace evolved trajectories for optimal torque estimation," in *Proc. IEEE/RSJ Int. Conf. Intell. Robots Syst.*, 2013, pp. 2370–2376.

[15] Z. Du, P. Iravani, and M. N. Sahinkaya, "A new approach to design optimal excitation trajectories for parameter estimation of robot dynamics," in *Proc. UKACC Int. Conf. Control*, 2014, pp. 389–394.
[16] J. Swevers, C. Ganseman, J. D. Schutter, and H. V. Brussel, "Experimental robot identification using optimised periodic trajectories," *Mech. Syst. Signal Process.*, vol. 10, no. 5, pp. 561–577, 1996.
[17] R. Luo, S. Bao, L. Du, Z. Hu, Y. Liu, and J. Yuan, "Optimal exciting trajectories for identifying dynamic parameters of serial robots," in *Proc. IEEE Int. Conf. Mechatron. Autom.*, 2023, pp. 1009–1014.
[18] M. M. Olsen, J. Swevers, and W. Verdonck, "Maximum likelihood identification of a dynamic robot model: Implementation issues," *Int. J. Robot. Res.*, vol. 21, no. 2, pp. 89–96, 2002.
[19] A. Jubien, M. Gautier, and A. Janot, "Dynamic identification of the kuka lightweight robot: Comparison between actual and confidential kuka's parameters," in *Proc. IEEE/ASME Int. Conf. Adv. Intell. Mechatron.*, 2014, pp. 483–488.
[20] J. Jin and N. Gans, "Parameter identification for industrial robots with a fast and robust trajectory design approach," *Robot. Comput.-Integr. Manuf.*, vol. 31, pp. 21–29, 2015.
[21] K.-J. Park, "Fourier-based optimal excitation trajectories for the dynamic identification of robots," *Robotica*, vol. 24, no. 5, pp. 625–633, 2006.
[22] W. Wu, S. Zhu, X. Wang, and H. Liu, "Closed-loop dynamic parameter identification of robot manipulators using modified Fourier series," *Int. J. Adv. Robot. Syst.*, vol. 9, no. 28, pp. 1–9, 2012.
[23] F. Shao and F. Ficuciello, "Dynamic parameter identification of the Kuka LBR med robot," in *Proc. IEEE Int. Conf. Automat. Sci. Eng.*, 2023, pp. 1–6.
[24] Y. Han, J. Wu, C. Liu, and Z. Xiong, "An iterative approach for accurate dynamic model identification of industrial robots," *IEEE Trans. Robot.*, vol. 36, no. 5, pp. 1577–1594, Oct. 2020.
[25] G. Calafiore, M. Indri, and B. Bona, "Robot dynamic calibration: Optimal excitation trajectories and experimental parameter estimation," *J. Robot. Syst.*, vol. 18, no. 2, pp. 55–68, 2001.
[26] S. Bethge, J. Malzahn, N. Tsagarakis, and D. Caldwell, "Flobaroid-A software package for the identification of robot dynamics parameters," in *Proc. Int. Conf. Robot. Alpe-Adria Danube Region*, 2018, pp. 156–165.
[27] X. Wu, B. Li, J. Wu, and Y. Zhu, "Optimization of the excitation trajectory of particle gray wolf optimization algorithm," in *Proc. IEEE Int. Conf. Mechatron. Autom.*, 2022, pp. 75–80.
[28] I. Rahimi, A. H. Gandomi, F. Chen, and E. Mezura-Montes, "A review on constraint handling techniques for population-based algorithms: From single-objective to multi-objective optimization," *Arch. Comput. Methods Eng.*, vol. 30, pp. 2181–2209, 2023.
[29] J. Swevers, W. Verdonck, and J. D. Schutter, "Dynamic model identification for industrial robots," *IEEE Control Syst. Mag.*, vol. 27, no. 5, pp. 58–71, Oct. 2007.
[30] H. N. Huynh, H. Assadi, E. Rivière-Lorphèvre, O. Verlinden, and K. Ahmadi, "Modelling the dynamics of industrial robots for milling operations," *Robot. Comput.-Integr. Manuf.*, vol. 61, 2020, Art. no. 101852.
[31] M. Jegorova, J. Smith, M. Mistry, and T. Hospedales, "Adversarial generation of informative trajectories for dynamics system identification," in *Proc. IEEE/RSJ Int. Conf. Intell. Robots Syst.*, 2020, pp. 7109–7115.
[32] X. Duan, Y. Wang, D. Romeres, T. Koike-Akino, and P. V. Orlik, "Trajectory generation for online payload estimation of robot manipulators: A supervised learning based approach," in *Proc. IEEE Int. Conf. Automat. Sci. Eng.*, 2023, pp. 1–7.
[33] R. V. Rao, V. J. Savsani, and D. P. Vakharia, "Teaching–learning-based optimization: A novel method for constrained mechanical design optimization problems," *Comput.-Aided Des.*, vol. 43, no. 3, pp. 303–315, 2011.
[34] R. V. Rao, *Teaching-Learning-Based Optimization Algorithm*. Cham, Switzerland: Springer, 2016.
[35] M. Tröbinger, A. Naceri, X. Chen, H. Sadeghian, and S. Haddadin, "Identification of a generalized base inertial parameter set of robotic manipulators considering mounting configurations," in *Proc. IEEE Int. Conf. Robot. Automat.*, 2023, pp. 11502–11508.
[36] Y. Dong, T. Ren, K. Chen, and D. Wu, "An efficient robot payload identification method for industrial application," *Ind. Robot.*, vol. 45, no. 4, pp. 505–515, 2018.
[37] Y. Huang, J. Ke, X. Zhang, and J. Ota, "Dynamic parameter identification of serial robots using a hybrid approach," *IEEE Trans. Robot.*, vol. 39, no. 2, pp. 1607–1621, Apr. 2023.
[38] S. Huang et al., "Robust estimation for an extended dynamic parameter set of serial manipulators and unmodeled dynamics compensation," *IEEE/ASME Trans. Mechatron.*, vol. 27, no. 2, pp. 962–973, Apr. 2022.
[39] G. Golluccio, G. Gillini, A. Marino, and G. Antonelli, "Robot dynamics identification: A reproducible comparison with experiments on the Kinova Jaco," *IEEE Robot. Autom. Mag.*, vol. 28, no. 3, pp. 128–140, Sep. 2020.
[40] C. D. Sousa and R. Cortesao, "Physical feasibility of robot base inertial parameter identification: A linear matrix inequality approach," *Int. J. Robot. Res.*, vol. 33, no. 6, pp. 931–944, 2014.
[41] J. Wu, J. Wang, and Z. You, "An overview of dynamic parameter identification of robots," *Robot. Comput.-Integr. Manuf.*, vol. 26, no. 5, pp. 414–419, 2010.
[42] Y. Zhou, Z. Li, X. Zhang, Y. Li, and M. Zhu, "A semilinearized approach for dynamic identification of manipulator based on nonlinear friction model," *IEEE Trans. Instrum. Meas.*, vol. 73, pp. 1–20, 2024.
[43] A. Raviola, R. Guida, A. D. Martin, S. Pastorelli, S. Mauro, and M. Sorli, "Effects of temperature and mounting configuration on the dynamic parameters identification of industrial robots," *Robotics*, vol. 10, no. 3, 2021, Art. no. 83.
[44] MATLAB R2020a, *Optim. Toolbox User's Guide*, Natick, MA, USA: MathWorks, 2014.
[45] D. P. Kingma and J. Ba, "Adam: A method for stochastic optimization," in *Proc. Int. Conf. Learn. Representations*, 2015.
[46] W. Khalil, M. Gautier, and P. Lemoine, "Identification of the payload inertial parameters of industrial manipulators," in *Proc. IEEE/RSJ Int. Conf. Intell. Robots Syst.*, 2007, pp. 4943–4948.
[47] C. D. Sousa and R. Cortesao, "Inertia tensor properties in robot dynamics identification: A linear matrix inequality approach," *IEEE/ASME Trans. Mechatron.*, vol. 24, no. 1, pp. 406–411, Feb. 2019.
[48] X. Yang, Z. Zhou, L. Li, and X. Zhang, "Collaborative robot dynamics with physical human–robot interaction and parameter identification with PINN," *Mech. Mach. Theory*, vol. 189, 2023, Art. no. 105439.
[49] C. Tan, H. Zhao, and H. Ding, "Identification of dynamic parameters of closed-chain industrial robots considering motor couplings," *Comput. Electr. Eng.*, vol. 99, 2022, Art. no. 107740.
[50] C. Wu, K. Guo, J. Sun, Y. Liu, and D. Zheng, "Active vibration control in robotic grinding using six-axis acceleration feedback," *Mech. Syst. Signal Process.*, vol. 214, 2024, Art. no, 111379.
[51] K. Rsetam, Z. Cao, and Z. Man, "Design of robust terminal sliding mode control for underactuated flexible joint robot," *IEEE Trans. Syst., Man, Cybern., Syst.*, vol. 52, no. 7, pp. 4272–4285, Jul. 2022.
[52] E. Wernholt and S. Gunnarsson, "Nonlinear identification of a physically parameterized robot model," *IFAC Proc.*, vol. 39, no. 1, pp. 143–148, 2006.
[53] H. Ni, C. Zhang, T. Hu, T. Wang, Q. Chen, and C. Chen, "A dynamic parameter identification method of industrial robots considering joint elasticity," *Int. J. Adv. Robot. Syst.*, vol. 16, no. 1, pp. 1–11, 2019.
[54] J. Kim and E. A. Croft, "Full-state tracking control for flexible joint robots with singular perturbation techniques," *IEEE Trans. Control Syst. Technol.*, vol. 27, no. 1, pp. 63–73, Jan. 2019.
[55] S. Ferrarini, P. Bilancia, R. Raffaeli, M. Peruzzini, and M. Pellicciari, "A method for the assessment and compensation of positioning errors in industrial robots," *Robot. Comput.-Integr. Manuf.*, vol. 85, 2024, Art. no. 102622.
[56] M. Schappler, J. Vorndamme, A. Todtheide, D. C. Conner, O. von Stryk, and S. Haddadin, "Modeling, identification and joint impedance control of the Atlas arms," in *Proc. IEEE-RAS Int. Conf. Humanoid Robots*, 2015, pp. 1052–1059.
[57] Y. Zhang, Y. Gao, and M. Sun, "Parameters identification of whole body dynamics for hexapod robot," in *Proc. IEEE Int. Conf. Robot. Biomimetics*, 2022, pp. 40–45.

Shifeng Huang (Member, IEEE) received the B.S. degree in mechanical design, manufacturing and automation from the Central South University, Changsha, China, in 2015, and the Ph.D. degree in mechanical engineering from the School of Mechanical Science and Engineering, Huazhong University of Science & Technology, Wuhan, China, in 2023.

He is currently a Postdoctoral Research Fellow with the Department of Mechanical and Aerospace Engineering, Hong Kong University of Science and Technology, Hong Kong. In addition, he serves as the deputy chief engineer at the Foshan Huashu Robot Co., Ltd. He focuses on the research of industrial and collaborative robots. His research interests include dynamics modeling and identification, time-optimal trajectory planning, physical human–robot interaction, motion control, vibration suppression.

Fan Li received the Ph.D. degree in industrial engineering from the School of Mechanical Science and Engineering, Huazhong University of Science & Technology, Wuhan, China. the B.Eng. degree in the mechanical design manufacture and automation from the School of Electromechanical and Architectural Engineering, Jianghan University, Wuhan, China, in 2015.

From 2021 to 2025, she was a Postdoctoral Research Fellow with the University of Exeter, Exeter, U.K. She is currently a Distinguished Associate Professor with the College of Mechanical and Electrical Engineering, Central South University, Changsha, China. Her research interests include multifidelity optimization, Bayesian optimization, multiobjective optimization, surrogate-assisted evolutionary optimization, and their applications to real-world engineering optimization problems.

Author Li was the recipient of the China Ministry of Education's Overseas Talent Introduction Program (National-level Youth Talent).

Xing Zhou received the B.S. and M.A. degrees in computer science, in 2004 and 2007, respectively, from the Huazhong University of Science & Technology, Wuhan, China, where he is currently working toward the Ph.D. degree in robot motion control and intelligent fault diagnosis.

He serves the Executive Vice President of the Foshan Institute of Intelligent Equipment Technology, Foshan City, China.

Dr. Zhou was the recipient of the First Prize of Science and Technology Progress of Hubei Province and China Patent excellence award once.

Molong Duan (Member, IEEE) received the B.S. degree in theoretical and applied mechanics from Peking University, Beijing, China, in 2012, and the M.S. and Ph.D. degrees in mechanical engineering from the Mechanical Engineering Department, University of Michigan, Ann Arbor, MI, USA, in 2013 and 2018, respectively.

He was granted the Rackham Centennial Fellowship from the University of Michigan, in 2013. He is currently an Assistant Professor with the Department of Mechanical and Aerospace Engineering, Hong Kong University of Science and Technology, Hong Kong. His research interests include the modeling and control of dynamic systems, robotic manufacturing vibration compensation, additive manufacturing control, continuous fiber additive manufacturing, flexible aircraft modeling and control, and VTOL aircraft modeling and control.

Dr. Duan was the recipient of the Best Poster Award at the 2014 International Forum on Sustainable Manufacturing, and the Best Student Paper Award at the 2015 Dynamic Systems and Controls Conference.